Probing the Subcellular Distribution of Phosphatidylinositol Reveals a Surprising Lack at the Plasma Membrane

James P. Zewe, April Miller, Sahana Sangappa, Rachel C. Wills, Brady D. Goulden* and Gerald R. V. Hammond

Department of Cell Biology, University of Pittsburgh School of Medicine, Pittsburgh, PA, USA.

*current address: Department of Cell Biology, Johns Hopkins University School of Medicine, Baltimore, MD, USA.

Running Title: Subcellular distribution of PI

Keywords: PtdIns; Lipids; Phospholipids;

Abstract

The polyphosphoinositides (PPIn) are central regulatory lipids that direct membrane function in eukaryotic cells. Understanding how their synthesis is regulated is crucial to revealing these lipids' role in health and disease. PPIn are derived from the major structural lipid, phosphatidylinositol (PI). However, although the distribution of most PPIn have been characterized, the subcellular localization of PI available for PPIn synthesis is not known. Here, we have used several orthogonal approaches to map the subcellular distribution of PI, including localizing exogenous fluorescent PI, as well as detecting lipid conversion products of endogenous PI after acute chemogenetic activation of PI-specific phospholipase and 4-kinase. We report that PI is broadly distributed throughout intracellular membrane compartments. However, there is a surprising lack of PI in the plasma membrane compared to the PPIn. These experiments implicate regulation of PI supply to the plasma membrane, as opposed to regulation of PPIn-kinases, as crucial to the control of PPIn synthesis and function at the PM.

Introduction

The polyphosphoinositides (PPIn) are crucial regulatory lipids in eukaryotic physiology. They direct protein localization and/or activation on the cytosolic face of membranes, thereby controlling myriad cellular processes such as membrane traffic, lipid exchange, ion transport, cell signaling and cytoskeletal dynamics (Balla, 2013; Dickson and Hille, 2019). Structurally, PPIn consist of phosphorylated derivatives of the major glycerophospholipid, phosphatidylinositol (PI). The enzymology of PPIn synthesis and turnover is well understood, and an important endeavor in cell biology seeks to understand the control of cellular physiology in both health and disease by understanding regulation of PPIn enzymes.

When considering their relative abundance, the PPIn have an outsized role in membrane function; they account for only ~2-10% of inositol lipid, with the remainder being PI (Anderson et al., 2013; Traynor-Kaplan et al., 2017). PI itself accounts for around 10% of total phospholipid (Vance, 2015), so it follows that PPIn constitute less than 1% of total phospholipid. On the other hand, PI is an important structural component of membranes, and its synthesis probably accounts for positive effects of dietary inositol supplementation, as opposed to effects on quantitatively minor PPIn (Michell, 2018).

PI is synthesized on the cytosolic face of the ER (Bochud and Conzelmann, 2015), from where some is “flopped” to the luminal leaflet for the synthesis of glycosylphosphatidylinositol-linked proteins (Vishwakarma et al., 2005). The remaining PI has been shown to be distributed fairly evenly across most organelle membranes by sub-cellular fractionation (Vance, 2015). However, in such studies, the fraction of PI in the cytosolic face of the membrane (and thus available for PPIn synthesis) is not known. Furthermore, the process of sub-cellular fractionation exposes membranes to phosphatases than can remove labile PPIn phosphate monoesters, consequently overestimating PI and underestimating PPIn. Therefore, it is currently unclear how much PI is available for PI synthesis in cytosolic membrane leaflets – and hence, whether the crucial regulatory step is the control of PI kinases activity, or supply of PI substrate.

A prominent example of this problem is at the plasma membrane (PM), which contains the majority of PI(4,5)P_2 and largest share of PI4P (Hammond and Balla, 2015). Although these lipids are ≤ 1% of total cellular phospholipid, they are specifically enriched at the PM, whereas the much more abundant PI is not; so PPIn likely account for a larger share of the PM inositol

lipid. How big a share? Estimates of the fraction of cellular phospholipids at the PM vary by two orders of magnitude, from 0.5% (Schmick et al., 2014) to 50% (Lange et al., 1989); assuming an intermediate fraction of 14% (Griffiths et al., 1989), PI(4,5)P_2 and PI4P may therefore be around ~7% of PM phospholipid, not far from the roughly 10% PI assumed if it were uniformly distributed among organelles including the PM. This fits with measurements of red blood cells, which only contain PM, where PI, PI4P and PI(4,5)P_2 are present in approximately equal quantities (Ferrell and Huestis, 1984). It also fits with observations from isolated cardiomyocyte PM, which has a limited supply of PI for PPIn re-synthesis after stimulation of phospholipase C (Nasuhoglu et al., 2002). In general though, there is scant evidence as to the relative abundance of PI in various organelles that is actually available for PPIn synthesis.

In this study, we have applied a series of distinct approaches to map the subcellular distribution of PI in intact, living cells. These included loading cells with fluorescent PI derivatives, and probing cells for diacylglycerol (DAG) and PI4P after inducing acute conversion of endogenous PI to these lipids. Whilst each approach carries significant caveats, collectively our results illustrate a wide subcellular distribution of PI, but a surprising lack at the PM.

Results

Intracellular distribution of exogenous fluorescent PI.

Lipids with fluorescent fatty acids have long been used as tracers for the traffic, metabolism and steady-state distribution of native lipids (Lipsky and Pagano, 1985; Struck and Pagano, 1980). In these experiments, exogenous lipids are applied to cells as either liposomes or via serum albumin carriers, from where they spontaneously incorporate into the exoplasmic leaflet of the PM. From here, the lipids follow the same cellular fate as the native molecules: they are either endocytosed, or else be flipped by native translocases. The flipped lipids may then traffic from the cytosolic leaflet of the PM to other organelles via vesicular and non-vesicular pathways, being metabolized along the way (Pagano et al., 1983). We attempted this approach with inositol lipids, using commercially available TopFluor®-fatty acid conjugated lipids. We reasoned this was a potentially viable approach, since native PI translocase and/or scramblase activities have been reported in mammalian cells, albeit with weaker activity compared to aminophospholipid translocases (Bütikofer et al., 1990; Wang et al., 2018).

We loaded COS-7 green monkey fibroblasts with TopFluor lipids using bovine serum albumin (BSA) for fifteen minutes before back-extracting the outer PM leaflet with excess BSA (figure 1A). As a positive control, we loaded cells with TopFluor-PS. This lipid rapidly incorporated into the PM and intracellular vesicles (figure 1A, top panel). It could not be back-extracted, since the PS is rapidly flipped to the inner leaflet by endogenous aminophospholipid translocases (figure 1A), exactly as described previously (Kay et al., 2012). On the other hand, TopFluor-PI(4,5)P_2 intensely labelled the plasma membrane, but was almost entirely back-extracted, leaving only punctate signal that presumably corresponded to endocytosed lipid in the exoplasmic leaflet (figure 1A, middle panel). The majority of TopFluor-PI was also back-extracted from the PM. However, in addition to the internalized vesicles, a substantial intracellular labelling appeared during loading that remained after back-extraction (figure 1A, bottom panel). This suggested that PI was indeed flipped into the inner PM leaflet, but in contrast to PS, was subsequently transported rapidly to other organelles.

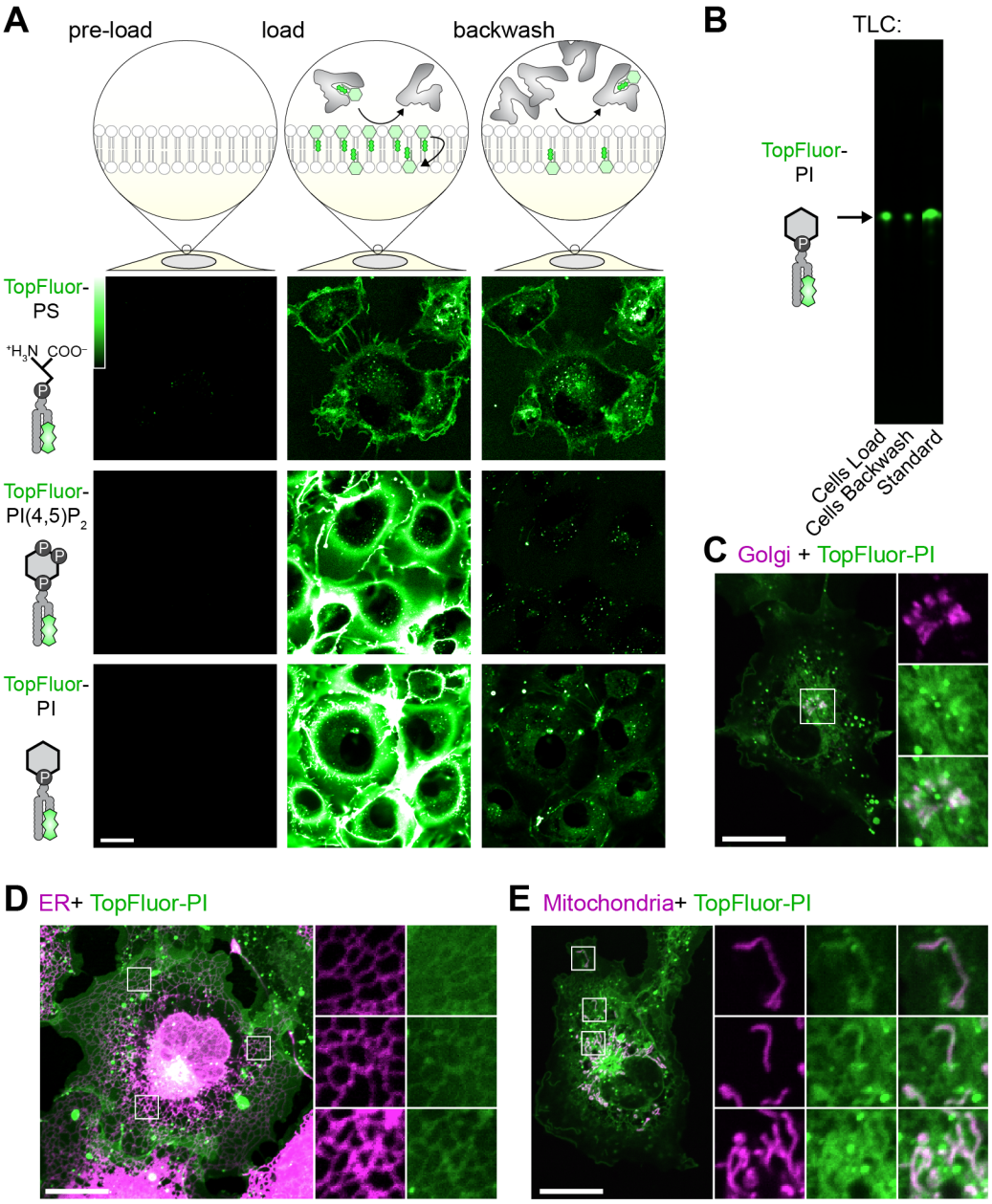

Figure 1: Fluorescent PI is not enriched at the PM. (**A**) **Internalization of fluorescent lipids**. COS-7 cells were loaded at 37˚C with the indicated acyl-conjugated TopFluor lipids complexed with BSA. After 15 min, a 20-fold excess of un-complexed BSA was used to back-extract lipid remaining in the outer PM leaflet. (**B**) **Loaded TopFluor-PI is not metabolized**. COS-7 cells were loaded or loaded and back-extracted as in A. Lipids were then extracted and resolved by thin-later chromatography. (**C-E**) **Loaded TopFluor-PI labels the Golgi** (C)**, ER** (D) **and mitochondria** (E). COS-7 cells that had been transfected with mCherry-β4-GalT^{N82} (C), iRFP-Sec61β (D) or COX8A^{N19}x2-mCherry (E) were loaded and back-extracted as in (A). Scale bar = 20 μm in all panels; insets are 10.9 μm (C) or 7.3 μm (D-E). Data are representative of three or more experiments.

Previous work has shown a similar, though much more rapid, translocation of NBD-labelled PI from the cell surface to intracellular membranes in 3T3 pre-adipocytes, though not in Chinese hamster ovary cells (Ting and Pagano, 1990). That rapid translocation was due to an exoplasmic phospholipase C activity in 3T3 cells that cleaved PI into the rapidly flip-flopping lipid, DAG. Therefore, we extracted lipids from our COS-7 cells loaded with TopFluor-PI before and after back extraction for analysis by thin-layer chromatography: we observed no such metabolism of PI, which migrated identically to the standard (figure 1B). Thus, COS-7 cells appeared to traffic exogenous fluorescent PI molecules from the PM and distribute it to intracellular membranes intact.

To identify these intracellular membranes, we performed high-resolution confocal microscopy of live cells expressing fluorescent protein conjugated markers of the most abundant intracellular membranes. With this approach, we could detect clear enrichment of the lipid at Golgi membranes (figure 1C), the endoplasmic reticulum (ER; figure 1D) and mitochondria (figure 1E). Surprisingly, relatively little TopFluor-PI was observed at the PM, in stark contrast to the observations with TopFluor-PS (figure 1A). This implies that PI is widely distributed in the cell, though notably absent from the PM, one of the most active compartments of phosphoinositide metabolism and function. However, these experiments still bear the significant caveat that the exogenous, derivatized PI may not reflect the endogenous distribution and traffic of native PI. They also do not furnish information on the transbilayer distribution of these lipids within the labelled organelles. For these reasons, we next turned our attention to approaches that could probe for the presence of endogenous PI in the cytoplasmic face of organelle membranes.

An acutely activatable PI-PLC to probe organelle PI content

In lieu of a bona fide PI biosensor for use in living cells, the PI-specific PLC from *Listeria monocytogenes* can be used as an indirect probe: the PI-PLC converts PI to inositol phosphate and DAG, the latter of which can then be detected with the selective, high affinity C1ab domain from PKD1 (Kim et al., 2011). The PI-PLC retains high activity despite its largely cytosolic localization, revealing highly dynamic DAG-containing structures that are not easily attributable to specific organelles of origin. However, prolonged exposure of cells to a degradative enzyme like a phospholipase risks extensive damage to membranes and activation of containment and repair processes. In other words, the DAG distribution may not closely reflect the intracellular

origin of the PI, which may have been generated several hours before imaging in these transfection experiments (Kim et al., 2011).

To circumvent this problem, we attempted to make an acutely activatable PI-PLC. Recruitment of lipid-modifying enzymes to membranes is one commonly used approach to accomplish this (DeRose et al., 2013), but the high basal activity of cytoplasmic PI-PLC (Kim et al., 2011) precluded this approach. We attempted to make mutants of *Bacillus cereus* PI-PLC with reduced (but not abolished) catalytic activity based on previously reported activity of the recombinant enzyme (Gässler et al., 1997). However, none of the mutants we screened retained sufficient activity to yield DAG production upon recruitment, whilst also showing low basal activity before recruitment. We also attempted to incorporate caged lysine into the *L. monocytogenes* enzyme using unnatural amino acids (Courtney and Deiters, 2018), though were unable to obtain expression of the mutated enzyme.

Finally, on inspecting the crystal structure of the *L. monocytogenes* enzyme, we noted that the protein consists of two well-defined amino and carboxy-terminal lobes with a single linking loop, and also possessed amino and carboxy termini that were close to one another (Moser et al., 1997). We therefore reasoned that the enzyme could be expressed as separate lobes that could be induced to form a functional enzyme after chemically-induced dimerization of FKBP (FK506-binding protein) and FRB (FKBP12 and Rapamycin binding domain of mTor) fused to the amino and carboxy terminal domains, respectively (figure 2A).

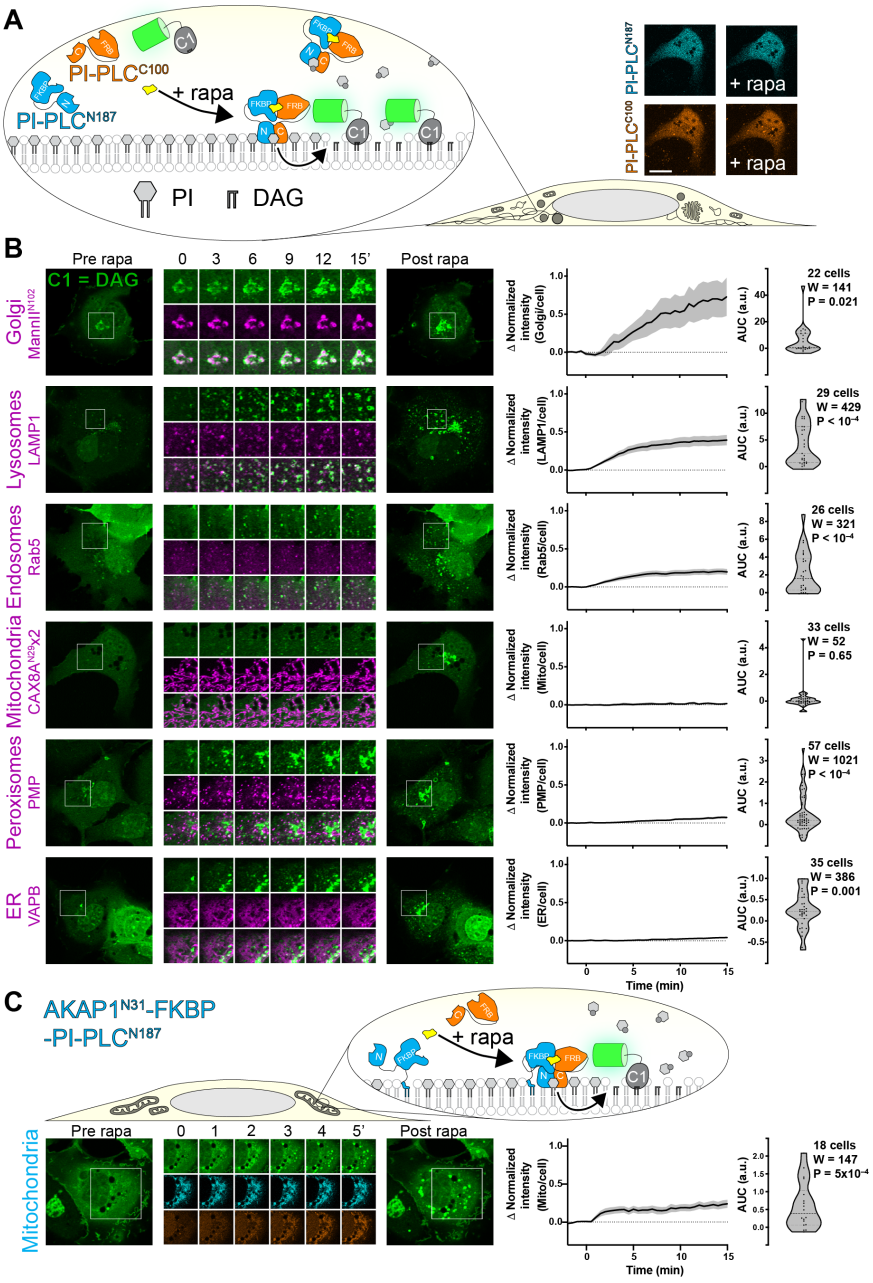

Figure 2: Chemically-induced dimerization of a split PI-PLC induces intracellular accumulation of DAG. (**A**) **Experimental set-up:** Rapamycin-induced dimerization of FKBP-fused N-terminal 187 residues of PI-PLC (cyan) with the FRB-fused C-terminal 100 residues (orange) reconstitutes the active enzyme, though no visible change in the cytosolic localization of the TagBFP2/iRFP-fused enzyme fragments is observed (confocal images at right). (**B**) **DAG accumulation on cytosolic leaflets of intracellular organelles**, with the greatest increases in the Golgi and endo/lysosomal compartments. Zero or comparatively minor changes were observed in mitochondria, peroxisomes or the ER. Cells were expressing GFP-PKD1-C1ab to detect DAG, the indicated organelle markers fused to mCherry or mKO (magenta), FKBP-PI-PLC^{N187} and FRB-PI-PLC^{C100} (not shown); they were treated with 1 μM rapamycin at time 0. Inset regions are 15 μm. (**C**) **Anchoring PI-PLC^{N187} to the mitochondrial outer membrane shows transient accumulation of DAG after recruitment of PI-PLC^{N100}**. Cells were transfected as in B, but with AKAP^{N31}—fused PI-PLC^{N187} replacing the unanchored version in B. In both B and C, the curves at right show the mean change in C1ab reporter intensity at each compartment, with s.e.m. shaded. The violin plots show area under the curve, with the number of cells (pooled across 3-6 independent experiments), the sum of signed ranks (W) and P-value from a two-tailed Wilcoxon signed rank test comparing to a null hypothesis area under the curve value of 0.

Expression of TagBFP2-FKBP-PLC^{N187} and PLC^{C100}-FRB-iRFP showed both enzymes distributed in the cytoplasm, as observed with the full-length enzyme (Kim et al., 2011); no change in localization was observed when dimerization was induced with rapamycin (see micrographs in figure 2A). However, a GFP-C1ab DAG biosensor expressed in the same cells began to show an intense juxtanuclear accumulation and many small, punctate structures in the cytoplasm (figure 2B). We identified many of these structures through co-localization with co-expressed organelle markers (figure 2B). The juxtanuclear accumulation occurred in and around the Golgi membranes marked by ManII^{N102}. Many of the cytoplasmic puncta showed co-localization with Rab5 or LAMP1 as markers of the early and endo/lysosomal compartments, respectively. Surprisingly, and in contrast to results with TopFluor-PI, we did not see substantial accumulation in the ER or mitochondria, nor peroxisomes. A small, statistically significant change in localization of C1ab fluorescence with peroxisomes and the ER was observed, though these may simply be due to chance overlap given the large increases in the number of cytoplasmic C1ab-labelled puncta. None seemed to precisely correspond to these organelles as they did for the Golgi and endosomes.

The most parsimonious explanation for our failure to observe PLC-mediated DAG generation at ER and mitochondria would that little PI remains in the cytosolic leaflets of these organelle membranes. However, it is also possible that the cytosolic enzyme is not active on these membranes. To more directly probe for the presence of PI substrate, we targeted the amino-terminal lobe of PI-PLC to the outer mitochondrial membrane by fusing it to the amino-terminal 31 amino acids of AKAP1 (Ma and Taylor, 2002), with the aim of recruiting the carboxyl-terminal half to reconstitute the enzyme at the organelle surface (figure 2C). Indeed, we could see robust recruitment of PLC^{C100}-FRB-iRFP, which now yielded a substantial increase in C1ab labelling of the mitochondria. Interestingly, although DAG appeared initially throughout the mitochondrial surface, the labelling rapidly resolved into small puncta. We do not know the nature of this re-localization of DAG, which could conceivably be phase separation or traffic of the accumulated lipid. It may, however, explain the failure to observe substantial labelling of the mitochondria by the cytosolic enzyme in our experiments (figure 2B) or previous studies (Kim et al., 2011).

We attempted similar experiments with the ER. However, fusion of PI-PLC^{N187} to the amino-terminal domain of STIM1 exhibited a mis-localized, punctate distribution in addition to the normal ER morphology, whereas fusion of PLC^{C100} to the SAC1 carboxy-terminal TM domains

failed to recruit cytosolic PI-PLC^{N187} (J.P.Z., R.W. and G.R.V.H., unpublished observations). Therefore, we were unable to definitively probe the cytosolic face of the ER with this approach.

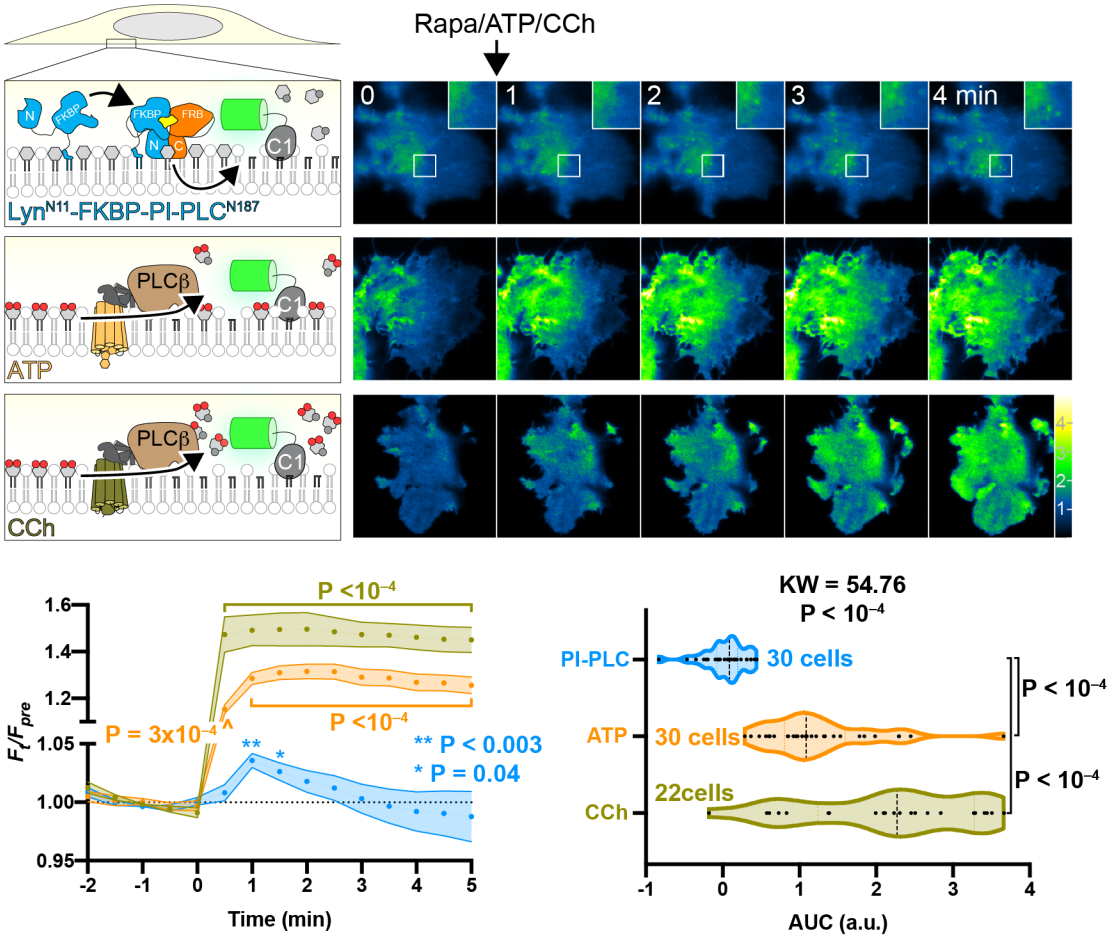

Figure 3: PM-specific dimerization of split PI-PLC induces very little DAG compared to PI(4,5)P$_2$-specific PLC. Cells were transfected with PI-PLC^{C100}-FRB, PM-targeted Lyn^{N11}-FKBP-PI-PLC^{N100} and GFP-PKD1-C1ab to detect DAG. Rapamycin was used to induce PI-PLC reconstitution at the PM, or else endogenous PLCβ was activated by G_q-coupled agonists ATP (to activate endogenous P2Y receptors) or carbachol (CCh, to activate over-expressed muscarinic M3 receptors). TIRFM images are color-coded to represent fluorescence intensity relative to pre-stimulus levels (F_t/F_{pre}) as indicated. Inset region is 5 μm. The line graphs show mean F_t/F_{pre} with s.e.m. shaded; P values are derived from Dunn's multiple comparison test comparing to time 0, following Friedman's test (Friedman statistic = 49.16, PI-PLC, P = 0.045; 497.0, ATP, P < 10^{-4}; 282.3, CCh; P < 10^{-4}). Where not indicated, the P value from Dunn's > 0.05. The violin plots show area under the curve analysis of the line graphs with the number of cells from 3 independent experiments, with results of a Kruskal-Wallis test and P values from a post-hoc Dunn's multiple comparison test indicated.

We also produced a PM-targeted PI-PLC^{N187} by fusion to the myristoylated and palmitoylated amino-terminal domain of Lyn kinase (figure 3). Dimerization with rapamycin induced the formation of a few C1ab-labelled puncta in these cells, visible by total internal reflection microscopy (TIRFM). Nonetheless, the overall increase in DAG was small and transient. In contrast, activation of PI(4,5)P$_2$-specific PLCβ by activation of either endogenous purinergic, or

over-expressed muscarinic M3 receptors caused a much larger increase in DAG (figure 3). This result would be consistent with the notion that in the PM, levels of PI are much lower compared to PI(4,5)P_2.

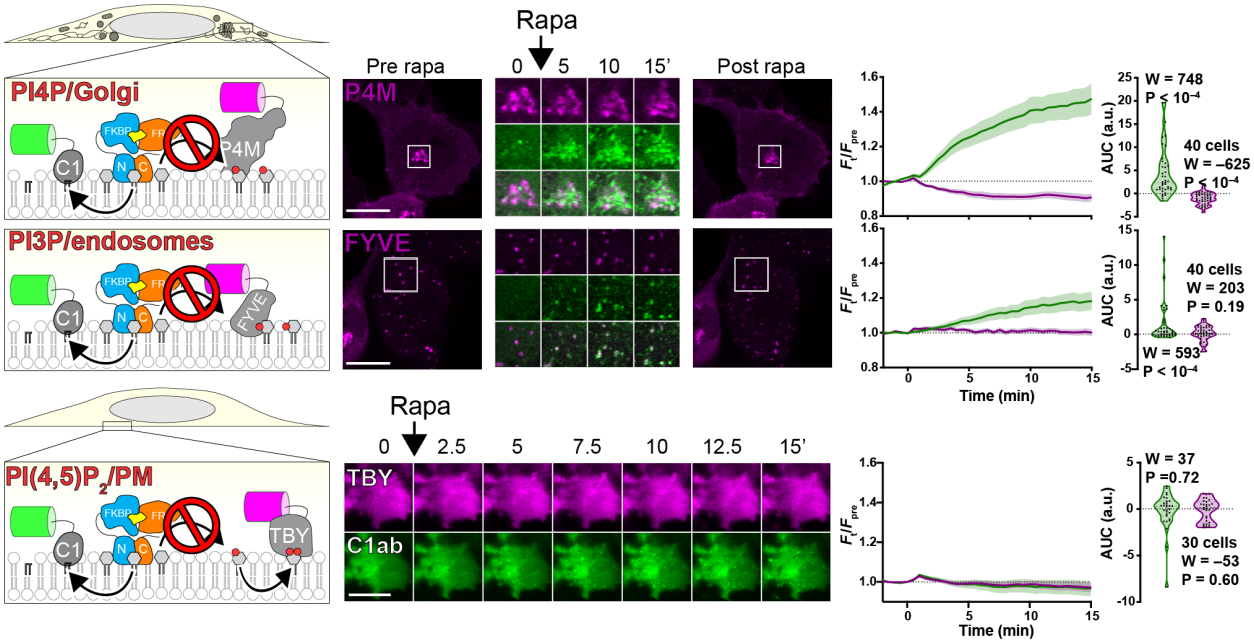

Figure 4: PI-PLC leads to little or no depletion of PPIn. Cells were transfected with PI-PLC^{C100}-FRB, FKBP-PI-PLC^{N100} (or PM-targeted Lyn^{N11}-FKBP-PI-PLC^{N100}) and GFP-PKD1-C1ab to detect DAG, along with the indicated PPIn biosensor. Dimerization and activation of PI-PLC was induced with 1 μM rapamycin as indicated. Images are confocal sections, except for the PM images which are TIRFM. Scale bars = 20 μm. Line graphs show the change in compartment specific fluorescence of C1ab (green) or the PPIn biosensor (magenta) normalized to pre-rapamycin levels (F_{pre}). The violin plots show area under the curve, with the number of cells (pooled across 3 independent experiments), the sum of signed ranks (W) and P-value from a two-tailed Wilcoxon signed rank test comparing to a null hypothesis area under the curve value of 0 (with a baseline of 1).

We also tested whether acute activation of PI-PLC reduced PI levels sufficiently to reduce levels of phosphoinositides, as was previously reported for constitutive over-expression of the intact enzyme (Kim et al., 2011). Notably, the large increase in C1ab after PI-PLC activation correlated with a partial depletion of Golgi-associated PI4P biosensor, P4M (figure 4). However, within 15 min we could not detect decreases in endosomal association of PI3P biosensor FYVE-EEA1 nor PM PI(4,5)P_2 biosensor Tubby$_c$. This could be interpreted as being due to a simple failure to sufficiently deplete the endosome or PM-associated PI levels. Alternatively, it would be consistent with the PI pools utilized in synthesis of these lipids being derived from other, non-PLC accessible sources that are not necessarily associated with these organelles.

Overall, these data demonstrate that PI is widely distributed in intracellular cytosolic membranes, though notably absent from the PM. These data are largely consistent with our observations of fluorescent PI re-distribution, though there were a number of differences, notably our failure to detect ER-associated PI. Therefore, we sought an alternative, corroborative approach.

Acute conversion to PI4P as a probe for PI

We reasoned we could also detect the presence of PI via conversion to PI4P after recruitment of a PI 4-OH kinase (PI4K), in a similar approach to detecting DAG derived from acutely re-constituted PI-PLC. To this end, we selected PI4KIIIα (encoded by *PI4KA*, referred to as PI4KA hereafter). The enzyme exists as a large, 700 kDa multi-subunit complex (Lees et al., 2017; Dornan et al., 2018); however, the isolated carboxy-terminal fragment containing the helical and catalytic domain ($PI4KA^{C1001}$) retains activity and can complement Hepatitis C proliferation in PI4KA knock-down cells (Harak et al., 2014). Therefore, we fused this fragment to FKBP to facilitate chemically induced dimerization with FRB, targeted to distinct organelle membranes (figure 5A). A catalytically inactive Asp^{1957} to Ala mutant served as a negative control. PI4P was detected with highly selective and unbiased probes for PI4P, namely the relatively low affinity P4M domain (Hammond et al., 2014) and the higher affinity P4C domain (Weber et al., 2014; Luo et al., 2015) from *Legionella* effectors SidM and SidC, respectively.

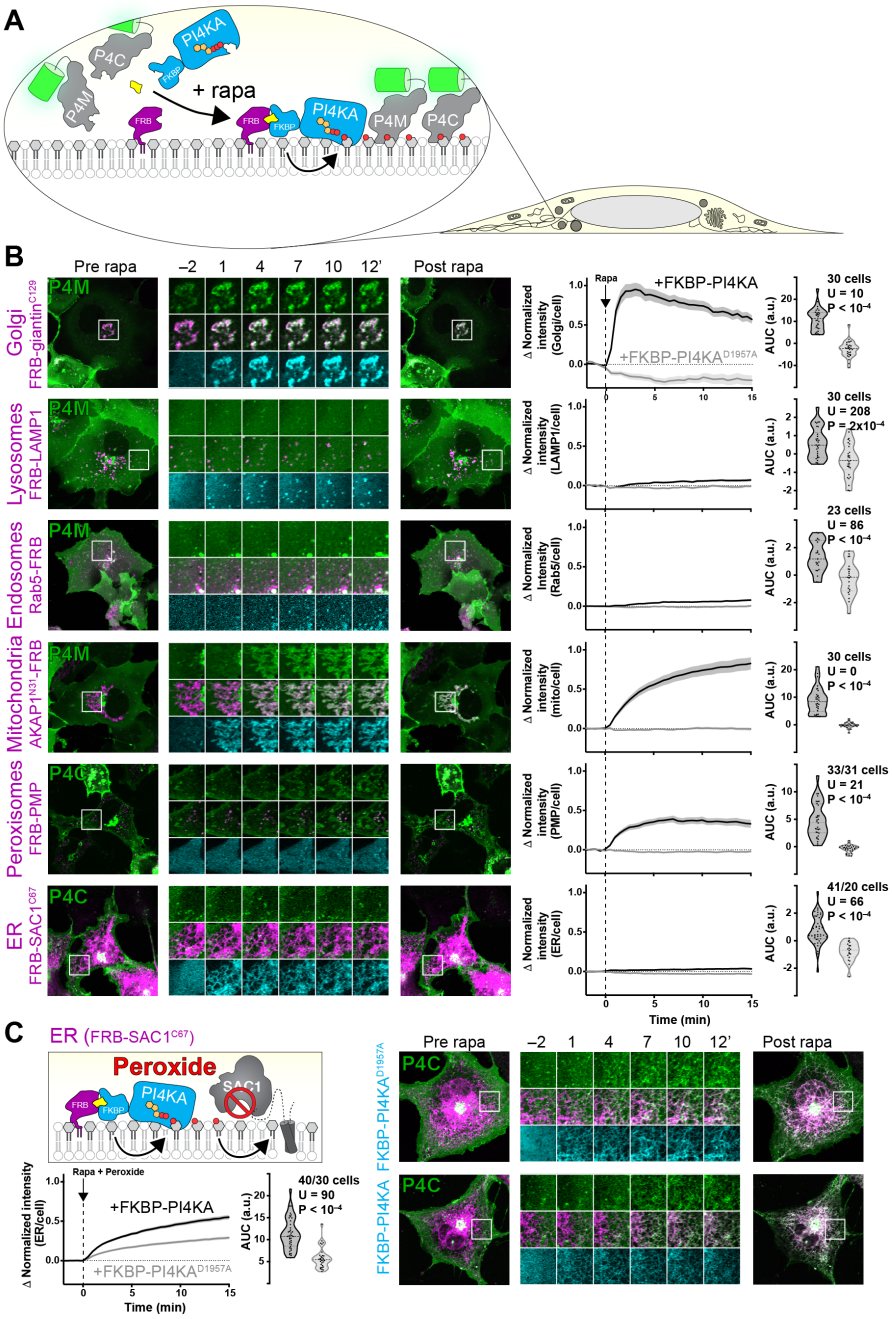

Figure 5: Compartment-specific recruitment of PI4KA reveals intracellular PI pools. (**A**) **Experimental set-up:** Rapamycin-induced recruitment of FKBP-PI4KA^{N1001} by dimerization with compartment-specific FRB to induce PI4P synthesis from endogenous PI, revealed with GFP-P4M or -P4C. (**B**) **PI4P accumulation on cytosolic leaflets of intracellular organelles**, with the greatest increases in the Golgi and mitochondria, with barely detectable increases in endosomes and ER. Peroxisomes show a large increase, but PI4P intensity also occurs outside of PMP-marked compartments. Cells are expressing GFP-P4M or -P4C (green), compartment-specific FRB (magenta) and FKBP-PI4KA^{N1001} (cyan) as indicated were treated with 1 μM rapamycin at time 0. Inset regions are 15 μm. The line graphs at right show the mean change in PI4P reporter intensity at each compartment, with s.e.m. shaded. The violin plots show area under the curve analysis of the curves, with the number of cells (pooled across 2-4 independent experiments), Mann-Whitney U statistic and P-value from a two-tailed test. (**C**) **Peroxide-mediated inhibition of ER-associated SAC1 PI4P phosphatase** reveals an endogenous pool of PI that can be converted to PI4P. Experiment and data are identical to (B), except cells were treated with 500 μM hydrogen peroxide in addition to rapamycin.

Recruitment of PI4KA^{C1001} to the Golgi induced a rapid and dramatic increase in PI4P levels at the Golgi (figure 5B), consistent with our observations with DAG after PI-PLC activation (figure 2B). Recruitment to Rab5- or LAMP1 positive endosomes and lysosomes produced a small but significant increase in PI4P, though this was less marked than the increases in DAG after PI-PLC activation (figure 2B). On the other hand, we could observe a dramatic increase in PI4P on the mitochondrial outer membrane when recruiting PI4KA^{C1001}, and a marked increase at peroxisomal membranes (figure 5B). Strangely, we noticed that in addition to producing PI4P in structures co-localizing with the peroxisomal FRB-PMP, an increase was also observed at a compartment with morphology consistent with mitochondria. We do not know if this is due to transfer of PI4P produced at peroxisomes to the mitochondrial outer membrane, perhaps via contact sites (Valm et al., 2017), or else direct synthesis of PI4P at mitochondrial membranes by a small pool of mis-targeted PMP.

We could barely detect PI4P synthesis at the ER after PI4KA^{C1001} recruitment (figure 5B). We reasoned that this was likely due to the presence of SAC1, a highly active PI4P phosphatase present throughout the ER (Zewe et al., 2018). Inhibition of SAC1 with peroxide causes rapid accumulation of PI4P at the ER, which has been interpreted as being due PI4P transfer from other organelles (Zewe et al., 2018). We therefore reasoned that recruitment of PI4KA^{C1001} during inhibition of SAC1 would cause a further increase in PI4P levels, due to conversion of any PI already present in the ER. Indeed, this is exactly what we observed: there was a substantial and highly significant increase in ER PI4P accumulation when active PI4KA^{C1001} was recruited relative to the inactive control (figure 4C). Therefore, we could corroborate the presence of PI in the ER suggested by the accumulation of TopFluor-PI there (figure 1D).

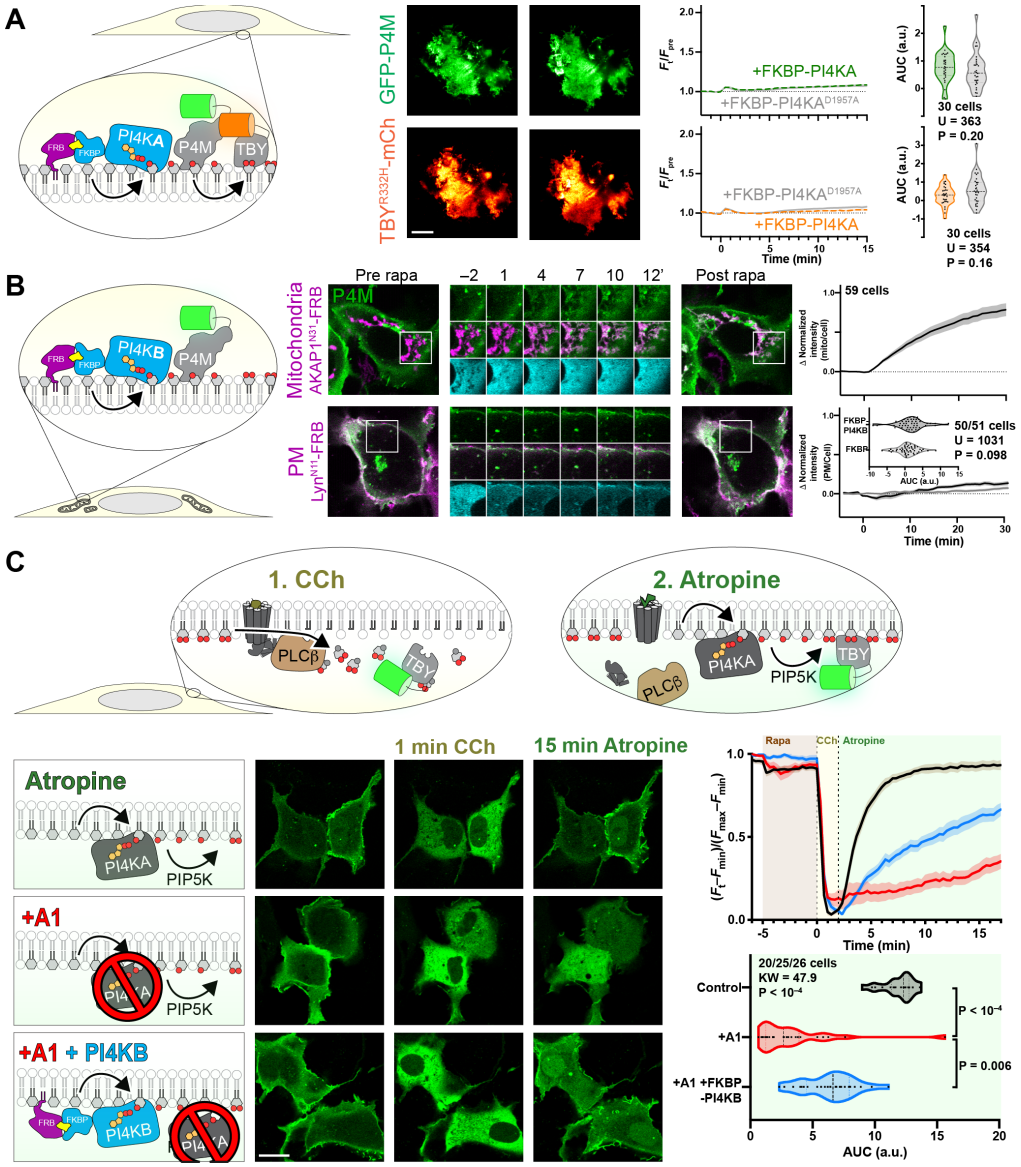

Figure 6: Recruitment of PI4K to the PM reveals a scarcity of PI. (**A**) **Recruitment of PI4KA^{N1001} shows no increase in PI4P or PI(4,5)P$_2$.** COS-7 cells imaged by TIRFM expressing GFP-P4Mx1 or Tubby$_c$-mCherry together with FKBP-PI4K^{N1001} and Lyn^{N11}-FRB were treated with 1 μM rapamycin at time 0 to induce dimerization. Scale bar = 20 μm. The curves at right show the mean change in reporter intensity, with s.e.m. shaded. The violin plots show area under the curve analysis of the curves, with the number of cells (pooled across 3 independent experiments) and the Mann-Whitney U statistic and P-value from a two-tailed test. (**B**) **PI4KB induces PI4P increases at the mitochondria but not the PM**. COS-7 cells were transfected with P4Mx1 to detect PI4P increases by confocal microscopy in conjunction with the indicated compartment-specific FRB and FKBP-PI4KB. Insets are 15 μm. Line graphs are means with s.e.m. shaded; inset violin plot shows area under the curve analysis, with number of cells (pooled across 3 independent experiments) and the Mann-Whitney U statistic and P-value from a two-tailed test. (**C**) **PI4KB is active in the PM**. COS-7 cells were co-transfected with PI(4,5)P$_2$ biosensor Tubby$_c$-GFP (green) and muscarinic M3 receptors, to stimulate PLCβ-induced PI(4,5)P$_2$ and PI4P depletion from the PM in response to carbachol treatment. Subsequent treatment with the muscarinic antagonist atropine induces re-synthesis of PI4P and PI(4,5)P$_2$ via endogenous PI4KA. Where indicated, the PI4KA inhibitor A1 was added at a 30 nM concentration. Images show confocal sections (bar = 20 μm) before stimulation, after addition of carbachol and after atropine addition as indicated. Curves are means with s.e.m. shaded. The violin plot shows area under the curve analysis for the post-atropine addition, with number of cells (three independent experiments), Kruskal-Wallis statistic and P value

from a two-tailed test. P values between individual groups show are derived from a post-hoc Dunn's multiple comparison test.

In contrast, we could detect no increases in PI4P at the PM by TIRFM after recruiting PI4KA^{C1001} (figure 6A), consistent with our observations with PI-PLC (figure 3) and the distribution of TopFluor-PI (figure 1). We also saw no increase in PI(4,5)P_2 detected with the low affinity Tubby c-terminal domain mutant, Tubby$_c^{R332H}$ (Quinn et al., 2008), ruling out conversion of extra PI4P to this lipid (figure 6A). An obvious interpretation of this result is that there is little PI resident in the PM available for conversion to PI4P (or to PI(4,5)P_2). However, we wanted to rule out other interpretations – specifically, that the PI4KA catalytic domain may be "biologically insufficient" to phosphorylate PI in the PM without assistance from PI transfer proteins (Grabon et al., 2015). To this end, we devised an experiment whereby the endogenous PM-associated PI4KA activity could be replaced with an alternative activity. For this purpose, we selected PI4KIIIβ (PI4KB), the isoform usually associated with PI4P synthesis at the Golgi (Balla and Balla, 2006). We made an FKBP fusion of this enzyme: recruitment to mitochondria caused accumulation of PI4P in this membrane (figure 6B), demonstrating the fusion was active. On the other hand, as we observed for FKBP-PI4KA^{C1001}, no increases in PI4P were observed after recruitment of FKBP-PI4KB to the PM relative to an FKBP-only control (figure 6B).

We next sought to demonstrate that PI4KB can intrinsically be active at the PM. One situation where a rapid increase in PM PI4P and PI(4,5)P_2 synthesis occurs is after recovery from PLCβ-mediated depletion of these lipids following muscarinic M3 acetylcholine receptor activation (Willars et al., 1998). We overexpressed M3 receptors in COS-7 cells expressing the Tubby c-terminal domain as a PI(4,5)P_2 reporter (figure 6C). Cells were stimulated with carbachol for 2 min to activate PLCβ, then the muscarinic antagonist atropine was added to shut off the PLC and facilitate PI(4,5)P_2 re-synthesis via PI4P (Nakanishi et al., 1995). Control cells rapidly re-synthesized PM PI(4,5)P_2 within four minutes (figure 6C). We then repeated this experiment whilst blocking the endogenous PI4KA activity with the highly potent and selective inhibitor A1 (Bojjireddy et al., 2014); very little re-synthesis of PI(4,5)P_2 occurs under these conditions (figure 6C). Finally, we repeated the A1 treatment in cells in which the A1-resistant FKBP-PI4KB was recruited to the PM: This led to a substantial recovery of PM PI(4,5)P_2 synthesis, though this was slower than in controls and incomplete in the 15 min period of the experimental recovery (figure 6C). Nonetheless, clear activity of PI4KB could be demonstrated in the PM – arguing

strongly that a failure to further increase PI4P (or PI(4,5)P_2) levels in unstimulated cells is due to a scarcity of PI available for conversion.

Discussion

In this paper, we performed experiments to map the subcellular distribution of PI in intact, living cells. We were particularly interested with respect to organelles that contain PPIn, since the availability of PI substrate for PPIn synthesis has important implications for the regulation of PPIn abundance and downstream physiology. We took three complimentary approaches: the localization of an exogenous, fluorescent PI (figure 1); localization of DAG, converted from PI by an acutely-activated PI-PLC (figures 2-4); and localization of PI4P, after acute conversion of PI by a membrane-recruited PI4K (figures 5-6). Broadly speaking, these approaches demonstrated the presence of PI in multiple intracellular membranes, but a relatively small amount (compared to PPIn) at the PM.

Each of the three approaches has significant caveats. Optical imaging of fluorescent lipids fails to give information as to the bilayer distribution, so does not necessarily reflect the PI available for conversion to PPIn by cytosolic PI kinases. Furthermore, the fluorescent moiety may disrupt the traffic and distribution of the exogenous lipid; for example, whereas TopFluor-labelled PS reflects closely the distribution of endogenous PS (Kay et al., 2012), NBD-labelled PS fails to show enrichment at the cytosolic face of the PM (Martin and Pagano, 1987).

On the other hand, acute conversion of PI to DAG or PI4P by acute chemogenetic activation of enzymes strictly reports endogenous, cytosolic leaflet-resident PI. Nevertheless, there are also substantial confounds to these experiments. Breakdown of a large fraction of phospholipid in a membrane to the much less polar DAG may dramatically alter bilayer properties (Alwarawrah et al., 2016). Moreover, DAG can readily flop to the exoplasmic leaflet (Bai and Pagano, 1997), or else be metabolized by DAG kinase, acyltransferases or lipases. Each process could significantly limit translocation of the C1ab domain probe, perhaps explaining the transient DAG accumulation observed at mitochondria before the signal resolves into a more punctate distribution (figure 2C). Likewise, acutely-induced PI4P could be subject to phosphorylation or dephosphorylation by PPIn enzymes, or else sequestration or transport by, for example, the OSBP-related family of proteins (Olkkonen, 2015). Indeed, the presence of the PI4P phosphatase Sac2 and the PI4P transfer protein OSBP at endosomes (Hsu et al., 2015;

Nakatsu et al., 2015; Dong et al., 2016) may explain our failure to induce significant PI4P accumulation at endosomes (figure 5B). Certainly, conditions wherein the ER-localized Sac1 phosphatase is limited allowed us to detect increased PI4P accumulation at the ER compared to conditions where native Sac1 was still active (figure 5C).

Our most consistent finding from all three approaches was that all failed to identify substantial PM-associated pools of PI. Although surprising, this observation is consistent with biochemical quantification from rapidly isolated PM sheets (Saheki et al., 2016). This finding is significant, in that it moves the onus for regulating PM PPIn synthesis from the PI4K-catalyzed PI phosphorylation to the supply of PI substrate for this enzyme.

The need for re-supply of ER-synthesized PI to the PM for PPIn synthesis has been known for a good many years (Lapetina and Michell, 1973). Vesicular transport of PI4P or PI from the Golgi, an organelle that we show is replete with both lipids, can contribute to PM PI(4,5)P_2 synthesis (Szentpetery et al., 2010; Dickson et al., 2014). However, these contributions do not explain the full capacity for PM synthesis, and the speed of the secretory pathway from the ER does not match the rate at which PM pools of PPIn can be turned over; instead, the activity of PI transfer proteins has been proposed to feed PPIn synthesis directly from the ER (Lapetina and Michell, 1973). More recently, specific PI transfer proteins such as Nir2 and TMEM24 have been identified in PM PPIn re-synthesis after activation of phospholipase C (Lees et al., 2017b; Dornan et al., 2018). Intriguingly, several of these studies found that simple over-expression of these transfer proteins can accelerate synthesis or elevate steady-state levels of PM PPIn (Chang et al., 2013; Kim et al., 2015; Lees et al., 2017a). Such observations are easily explained when viewed through the prism of our findings, which demonstrate a limited supply of PI at the PM; expanding the supply process is thus expected to increase synthesis or steady-state levels. However, they do not explain how cells control steady-state PI4P and PI(4,5)P_2 accumulation. Recently, a regulatory mechanism that puts a break on PI4P catabolism at the PM when levels of PI(4,5)P_2 drop has been demonstrated (Sohn et al., 2018). However, what homeostatic mechanism(s) maintain steady state levels of PI(4,5)P_2, and how this mechanism couples to the transport of PI to the PM, is a significant question for the future.

Materials and Methods

Plasmids and Cloning

Production of new plasmids for this study was accomplished by standard restriction-ligation or NEBuilder HiFi DNA Assembly (New England Biolabs E5520S), typically using Clontech pEGFP-C1 and -N1 backbones or their derivatives. Our standard fluorophores were a human codon optimized EGFP derived from *Aequorea victoria* GFP containing F64L and S65T mutations (Cormack et al., 1996), a *Discoma* DsRed monomeric variant known as mCherry (Shaner et al., 2004), the iRFP variant derived from *Rhodopseudomonas palustris* bacteriophytochrome BphP2 (Filonov et al., 2011), and mTagBFP2 derived from *Entacmaea quadricolor* protein eqFP578 (Subach et al., 2011). Mutated constructs were generated by site-directed mutagenesis using targeted pairs of DNA oligos. All custom oligos were supplied by ThermoFisher. After cloning, all constructs were sequence verified by Sanger DNA sequencing. Plasmids constructed for this study are available through Addgene (www.addgene.org). The table below lists all plasmids used in this study and their respective sources:

Plasmid	Vector	Insert	Reference
NES-EGFP-P4Mx1	pEGFP-C1	*X.leavis map2k1.L(32-44):EGFP:L. pneumophila SidM(546-647)*	(Sohn et al., 2018)
Lyn^{N11}-FRB-iRFP	piRFP-N1	*LYN(1-11):MTOR(2021-2113):iRFP*	(Hammond et al., 2014)
LAMP1-FRB-iRFP	piRFP-N1	*LAMP1:MTOR(2021-2113):iRFP*	(Goulden et al., 2018)
EGFP-FYVE-EEA1	pEGFP-C1	*EGFP:EEA1(1253-1411)*	(Balla et al., 2000)
NES-EGFP-P4Mx1	pEGFP-C1	*X.leavis map2k1.L*(32-44):EGFP:*L. pneumophila SidM*(546-647)	(Zewe et al., 2018)
mCherry-Rab5	pmCherry-C1	*mCherry:Canis lupus RAB5A*	(Hammond et al., 2014)
iRFP-N1-PI-PLC^{C100}-FRB	piRFP-N1	*L. monocytogenes PI-PLC(188-287)*:IGTAGPRSANS[GA]$_4$*: MTOR(2021-2113):iRFP*	(This study)
TagBFP2-C1-FKB-PI-PLC^{N187}	pTagBFP-C1	*TagBFP2:FKBP1A(3-108)*:[GGSA]$_4$GG*:L. monocytogenes PI-PLC(1-187)*	(This study)
pTagBFP2-C1-lynN^{11}-FKBP-PI-PLC^{N187}	pTagBFP-C1	*LYN(1-11)*:RSANS[GA]$_4$*:TagBFP2: FKBP1A(3-108):* [GGSA]$_4$GG*:L. monocytogenes PI-PLC(1-187)*	(This study)

pTagBFP2-C1-AKAP1^{N31}-FKBP-PI-PLC^{N187}	pTagBFP-C1	*Mus musculus Akap1*(1-31) M16L: PTRSANS[GA]$_4$ILSRM*:TagBFP2: FKBP1A(3-108):* [GGSA]$_4$GG*:L. monocytogenes PI-PLC(1-187)*	(This study)
mCherry-Rab7	pmCherry-C1	*mCherry:Canis lupus RAB7A*	(Hammond et al., 2014)
mCherry-FKBP-PI4KB	pmCherry-C1	mCherry: *TagBFP2: FKBP1A(3-108):* GGSA]$_4$GG*:PI4KB*	(This Study)
mCherry-FKBP-PI4KA^{C1001}	pmCherry-C1	mCherry: *TagBFP2: FKBP1A(3-108):* GGSA]$_4$GG*:PI4KA(1102-2103)*	(This Study)
piRFP-FRB-Giantin	piRFP-C1	iRFP:*MTOR*(2021-2113):[GGSA]$_2$:*GOLGB1*(3097-3226)	(This study)
pmCherry-C1ab-Prkd1	pmCherry-C1	mCherry:*Mus musculus Prkd1*(138-343)	(This study)
NES-GFP-C1ab-Prkd1	pEGFP-C1	EGFP:*Mus musculus Prkd1*(138-343)	(Kim et al., 2011)
Tubby$_c$-mCherry	pEGFP-N1	*Mus musculus Tub*(243-505):mCherry	(Quinn et al., 2008)
Tubby$_c^{R332H}$-mCherry	pEGFP-N1	*Mus musculus Tub*(243-505) R332H:mCherry	(Quinn et al., 2008)
Akap1(31)-FRB-iRFP	piRFP-N1	*Mus musculus Akap1*(1-31) M16L:*MTOR(2021-2113):iRFP*	(This study)
piRFP-FRB-PMP-C-10	piRFP-C1	iRFP: *MTOR*(2021-2113):[GGSA]$_2$QASNSAVSGLRSGSSGG:*PXMP*(2-195)	(This study)
iRFP-FRB-ER	piRFP-C1	iRFP:*MTOR*(2021-2113):[GGSA]$_2$ILNSRV:*SACM1L*(521-587)	(This study)
β4-GalT^{N82}-mCherry	pmCherry-N1	*B4GALT*(1-82):mCherry	Addgene #55052*
iRFP-Sec61β	piRFP-C1	iRFP:*SEC61B*	(Zewe et al., 2018)
COX8A^{N29}x2-mCherry	pmCherry-N1	*COX8A*(1-29):mCherry	This study
MannII^{N21}-mKO2	pmKO2-N1	*Mus musculus Man2a*(1-102):*Kusabira Orange2:*	Addgene #57881*
LAMP1-mRFP	pmRFP-N1	*LAMP1:mRFP*	(Jović et al., 2012)
mCherry-PMP	pmCherry-C1	mCherry:SGLRSRAQASNSAV:*PXMP*(2-195)	
mCherry-VAPB	pmCherry-C1	mCherry:*VAPB*	(Zewe et al., 2018)
HAx3-AChR-M3	pcDNA3.1	HAx3:CHRM3(2-590)	J.Wes

*B4-GalT^{N82}-mCherry (Addgene plasmid #55052; RRID:Addgene_55052) and MannII^{N21}-KO2 (Addegene plasmid #57881; RRID:Addgene_57881) were gits from Michael Davidson.

Chemicals and Reagents

For chemical dimerization experiments, Rapamycin (Fisher Scientific BP2963-1) was dissolved to 1 mM in DMSO as a stock and used at a final concentration of 1 μM in cells. Carbachol (Fisher Scientific AC10824-0050) was prepared by dissolving in water to 50 mM and stored at -20°C. Atropine (Fisher Scientific AC226680100) was dissolved to 25 mM in 100% ethanol and stored at -20°C. 30% H_2O_2 (EMD Millipore HX0635-3) was stored at 4°C and prepared fresh in complete imaging media when used as an additive. A1 PI4KA inhibitor (Bojjireddy et al., 2014), a kind gift from Tamas Balla, was dissolved in DMSO to a 100 μM stock and stored at -20°C.

Cell Culture and Lipofection

COS-7 (ATCC CRL-1651) cells were cultured at 37°C with a humidified 5% CO_2 atmosphere in low glucose DMEM (ThermoFisher 10567022) supplemented with 10% heat-inactivated fetal bovine serum (ThermoFisher 10438-034), 100 units/mL Penicillin-Streptomycin (ThermoFisher 15140122) and 0.1% chemically defined lipid supplement (ThermoFisher 11905031). Cells were passaged two times a week 1:5 in culture-treated flasks using TrypLE dissociation media (ThermoFisher 12604039).

In preparation for imaging, cells were seeded onto 35 mm #1.5 cover glass bottom dishes (CellVis D35-20-1.5-N) pre-coated with 5 μg of human fibronectin (ThermoFisher 33016-015) dissolved in water. Once adherent and between 50% - 80% confluent, cells were transfected according to manufacturer's instructions using 1 μg of total DNA complexed with 3 μg Lipofectamine2000 (ThermoFisher 11668019) in 200 μL Opti-MEM (ThermoFisher 51985091). Imaging of transfected samples occurred after an incubation time of ~18-24 hr.

Fluorescent Lipids

TopFluor® conjugated PI, PS, and PI(4,5)P_2 were obtained from Avanti Polar Lipids Inc. (810187P, 810283P, 810184P). Lipid-BSA complexing was accomplished using 5 μM (0.34 mg/ml) fatty acid-free BSA (Sigma 126575) dissolved in PBS with 3 mM EGTA. Fluorescent lipids were sonicated in methanol at a concentration of 1 mM before injecting 5 μl into 1 ml BSA/PBS mixture and vortexed at medium to high speed and incubated at 37°C for 20-30 min. Back-extraction media was made using 17 mg/mL fatty acid-free BSA (i.e. 250 μM, 5 x the final concentration applied to cells) in serum-free imaging media and filtered.

Thin-layer Chromatography

LK6D 60 Å silica gel 20 x 20 cm glass-backed TLC plates (Whatman 4865-821) were prepared by dipping into 74 mM sodium oxalate in 0.5% boric acid and dried overnight. Before loading, plates were pre-equilibrated in a 70:70:4:16 chloroform, methanol, ammonium hydroxide and water mixture. After loading, the plates were run in the same solvent mixture, then removed and allowed to dry for 15 min at room temperature in a fume hood. Fluorescent lipids were imaged using a ChemiDoc MP imaging system (BioRad) using 460-490 nm LED epi-illumination and a 518-546 nm emission filter.

Cells were extracted using a modified protocol (LEES et al., 1959). Briefly, cells in 35 mm glass bottom dishes were lysed in 250 μl 1 M HCl, scraped and collected in polypropylene tubes. The dishes were rinsed with 333 μl methanol, which was then pooled with the HCl extract. 667 μl chloroform was then added to the extracts before samples were vortexed vigorously and centrifuged to resolve two phases. The lower phase was removed and washed with 3:48:47 chloroform:methanol:1M HCl, and the upper phase re-extracted with 86:14:1 chloroform:methanol:1M HCl. After re-centrifuging to resolve phases, the washed lower phase was transferred to a fresh polypropylene tube, and the re-extracted upper phase was washed. This washed re-extract was pooled with the original extract and dried under nitrogen. Samples were re-dissolved in 30 μL of a 86:14:1 mixture of chloroform, methanol and 1M HCl and streaked into the concentration zone of the TLC plate to run.

Microscopy

For all live-cell imaging, standard growth medium was replaced with Fluorobrite DMEM (ThermoFisher A1896702) supplemented with 10% heat-inactivated fetal bovine serum, 25mM HEPES (pH 7.4), 0.1% chemically defined lipid supplement and 2 mM Glutamax (ThermoFisher 35050061). Initial volume of imaging media was adjusted so that 2 mL total volume was achieved after all chemical additions for a given experiment.

Confocal imaging was accomplished on a Nikon TiE A1R platform acquiring images in resonant mode with a 100X 1.45 NA plan-apochromatic objective. Signal to noise ratio was improved by taking 8 frame averages. Excitation of fluorophores was accomplished via a dual fiber-coupled LUN-V laser launch with 405 nm (BFP), 488 nm (GFP), 561 nm (mCherry) and 640nm (iRFP) lines. Emission was collected through dual pass filters from Chroma: blue/yellow-orange (420-480 nm / 570-620 nm) and green/far-red (505-550 nm / 650-850 nm). Confocal pinhole size was defined as 1.2X the Airy disc size of the longest wavelength channel used in the experiment. Nikon Elements software was used to acquire images for all experiments. All data were saved with the file extension .nd2.

An independent Nikon TiE platform coupled with a TIRF illuminator arm (Nikon) and 100X 1.45 NA plan-apochromatic objective was used to acquire TIRFM imaging data. Excitation of fluorophores was accomplished via an Oxxius L4C laser launch with 405nm (BFP), 561nm (mCherry) and 638nm (iRFP) lines. Emission was collected through dual pass filters from

Chroma: blue/yellow-orange (420-480 nm / 570-620 nm) and green/far-red (505-550 nm / 650-850 nm). A Zyla 5.5 sCMOS camera (Andor) was used to capture images, binning 2X2. Nikon Elements software was used to acquire images for all experiments. All data were saved with the file extension .nd2.

Image Analysis

Analysis of images was accomplished in Fiji software (Schindelin et al., 2012). A custom macro was written to generate channel-specific montages and display all xy positions captured in a given experiment in concatenated series. Individual regions of interest (ROI) were then generated around cells displayed in these montages.

The ratio of fluorescence intensity between specific compartments in confocal images were analyzed as described previously (Zewe et al., 2018). A custom macro was used to generate a binary mask through à trous wavelet decomposition (Olivo-Marin, 2002). The mask was applied to measure fluorescence intensity within a given compartment, while normalizing to the ROI's mean pixel intensity to account for variance in expression level present in transient transfections.

To analyze TIRFM images, a minimum intensity projection was used as the basis to generate ROIs within the footprint of individual cells. Background fluorescence values were measured and subtracted from images at all time-points. Fluorescence values were then normalized to the ROI's mean pixel intensity of time-points preceding treatment or stimulation.

For statistical analysis and generation of graphs and plots, quantitative data was imported into Prism 8 (GraphPad). For area under the curve (AUC) analysis, baseline-corrected data were first sorted into groups of individual curves. The net area under the curve for each ROI was then pooled and compared among conditions. D'Agostino and Pearson normality tests returned values that significantly varied from a normal distribution, so data were subjected to a non-parametric Kruskal-Wallis test and if significant variance between medians was found, Dunn's multiple comparisons test was run post-hoc.

All representative images were selected based on a robust signal to noise ratio, typical morphology and fluorescence measurements near the median of its cohort. Any adjustments

made to brightness or contrast to ease visibility were made in a linear fashion across the entire image.

Acknowledgments

We thank colleagues cited in the Materials and methods for generously sharing plasmids. This work was supported by National Institutes of Health grant 1R35GM119412-01 (to G.R.V.H.).

Author Contributions

J. P. Zewe, R. C. Wills, B.D. Goulden, G.R.V. Hammond conceived of the experiments and developed methods. J.P. Zewe, A. Miller, S. Sangappa, R. C. Wills and G.R.V. Hammond performed experiments. J.P. Zewe, A. Miller, S. Sangappa, R. C. Wills and G.R.V. Hammond analyzed data. G.R.V. Hammond acquired grant funding for this study. G.R.V. Hammond wrote the original draft of the manuscript; All authors reviewed and edited the manuscript.

References

Alwarawrah M, Hussain F, Huang J. 2016. Alteration of lipid membrane structure and dynamics by diacylglycerols with unsaturated chains. *Biochimica Et Biophysica Acta Bba - Biomembr* **1858**:253–263. doi:10.1016/j.bbamem.2015.11.014

Anderson KE, Kielkowska A, Durrant TN, Juvin V, Clark J, Stephens L, Hawkins PT. 2013. Lysophosphatidylinositol-Acyltransferase-1 (LPIAT1) Is Required to Maintain Physiological Levels of PtdIns and PtdInsP2 in the Mouse. *PLoS ONE* **8**:e58425. doi:10.1371/journal.pone.0058425

Bai J, Pagano RE. 1997. Measurement of Spontaneous Transfer and Transbilayer Movement of BODIPY-Labeled Lipids in Lipid Vesicles†. *Biochemistry-us* **36**:8840–8848. doi:10.1021/bi970145r

Balla A, Balla T. 2006. Phosphatidylinositol 4-kinases: old enzymes with emerging functions. *Trends in Cell Biology* **16**:351–361. doi:10.1016/j.tcb.2006.05.003

Balla T. 2013. Phosphoinositides: Tiny Lipids With Giant Impact on Cell Regulation. *Physiological Reviews* **93**:1019–1137. doi:10.1152/physrev.00028.2012

Balla T, Bondeva T, Várnai P. 2000. How accurately can we image inositol lipids in living cells? *Trends Pharmacol Sci* **21**:238–241. doi:10.1016/s0165-6147(00)01500-5

Bochud A, Conzelmann A. 2015. The active site of yeast phosphatidylinositol synthase Pis1 is facing the cytosol. *Biochimica et Biophysica Acta (BBA) - Molecular and Cell Biology of Lipids* **1851**. doi:10.1016/j.bbalip.2015.02.006

Bojjireddy N, Botyanszki J, Hammond G, Creech D, Peterson R, Kemp DC, Snead M, Brown R, Morrison A, Wilson S, Harrison S, Moore C, Balla T. 2014. Pharmacological and Genetic Targeting of the PI4KA Enzyme Reveals Its Important Role in Maintaining Plasma Membrane Phosphatidylinositol 4-Phosphate and Phosphatidylinositol 4,5-Bisphosphate Levels. *J Biol Chem* **289**:6120–6132. doi:10.1074/jbc.m113.531426

Bütikofer P, Lin Z, Chiu D, Lubin B, Kuypers F. 1990. Transbilayer distribution and mobility of phosphatidylinositol in human red blood cells. *The Journal of biological chemistry* **265**:16035–8.

Chang C-L, Hsieh T-S, Yang TT, Rothberg KG, Azizoglu BD, Volk E, Liao J-C, Liou J. 2013. Feedback Regulation of Receptor-Induced Ca2+ Signaling Mediated by E-Syt1 and Nir2 at Endoplasmic Reticulum-Plasma Membrane Junctions. *Cell Reports* **5**:813–825. doi:10.1016/j.celrep.2013.09.038

Cormack BP, Valdivia RH, Falkow S. 1996. FACS-optimized mutants of the green fluorescent protein (GFP). *Gene* **173**:33–38. doi:10.1016/0378-1119(95)00685-0

Courtney T, Deiters A. 2018. Recent advances in the optical control of protein function through genetic code expansion. *Curr Opin Chem Biol* **46**:99–107. doi:10.1016/j.cbpa.2018.07.011

DeRose R, Miyamoto T, Inoue T. 2013. Manipulating signaling at will: chemically-inducible

dimerization (CID) techniques resolve problems in cell biology. *Pflügers Archiv - European Journal of Physiology* **465**:409–417. doi:10.1007/s00424-012-1208-6

Dickson EJ, Hille B. 2019. Understanding phosphoinositides: rare, dynamic, and essential membrane phospholipids. *The Biochemical journal* **476**:1–23. doi:10.1042/BCJ20180022

Dickson EJ, Jensen JB, Hille B. 2014. Golgi and plasma membrane pools of PI(4)P contribute to plasma membrane PI(4,5)P2 and maintenance of KCNQ2/3 ion channel current. *Proc National Acad Sci* **111**:E2281–E2290. doi:10.1073/pnas.1407133111

Dong R, Saheki Y, Swarup S, Lucast L, Harper WJ, De Camilli P. 2016. Endosome-ER Contacts Control Actin Nucleation and Retromer Function through VAP-Dependent Regulation of PI4P. *Cell* **166**:408–423. doi:10.1016/j.cell.2016.06.037

Dornan GL, Dalwadi U, Hamelin DJ, Hoffmann RM, Yip CK, Burke JE. 2018. Probing the Architecture, Dynamics, and Inhibition of the PI4KIIIα/TTC7/FAM126 Complex. *J Mol Biol* **430**:3129–3142. doi:10.1016/j.jmb.2018.07.020

Ferrell J, Huestis W. 1984. Phosphoinositide metabolism and the morphology of human erythrocytes. *The Journal of cell biology* **98**:1992–1998. doi:10.1083/jcb.98.6.1992

Filonov GS, Piatkevich KD, Ting L-M, Zhang J, Kim K, Verkhusha VV. 2011. Bright and stable near-infrared fluorescent protein for in vivo imaging. *Nature Biotechnology* **29**:757–761. doi:10.1038/nbt.1918

Gässler CS, Ryan M, Liu T, Griffith HO, Heinz DW. 1997. Probing the Roles of Active Site Residues in Phosphatidylinositol-Specific Phospholipase C fromBacillus cereusby Site-Directed Mutagenesis†. *Biochemistry-us* **36**:12802–12813. doi:10.1021/bi971102d

Goulden BD, Pacheco J, Dull A, Zewe JP, Deiters A, Hammond G. 2018. A high-avidity biosensor reveals plasma membrane PI(3,4)P2 is predominantly a class I PI3K signaling product. *J Cell Biol*. doi:10.1083/jcb.201809026

Grabon A, Khan D, Bankaitis VA. 2015. Phosphatidylinositol transfer proteins and instructive regulation of lipid kinase biology. *Biochimica et Biophysica Acta (BBA) - Molecular and Cell Biology of Lipids* **1851**:724–735. doi:10.1016/j.bbalip.2014.12.011

Griffiths G, Back R, Marsh M. 1989. A quantitative analysis of the endocytic pathway in baby hamster kidney cells. *J Cell Biology* **109**:2703–2720. doi:10.1083/jcb.109.6.2703

Hammond G, Balla T. 2015. Polyphosphoinositide binding domains: Key to inositol lipid biology. *Biochimica et Biophysica Acta (BBA) - Molecular and Cell Biology of Lipids* **1851**:746–758. doi:10.1016/j.bbalip.2015.02.013

Hammond G, Machner MP, Balla T. 2014. A novel probe for phosphatidylinositol 4-phosphate reveals multiple pools beyond the Golgi. *J Cell Biology* **205**:113–126. doi:10.1083/jcb.201312072

Harak C, Radujkovic D, Taveneau C, Reiss S, Klein R, Bressanelli S, Lohmann V. 2014. Mapping of Functional Domains of the Lipid Kinase Phosphatidylinositol 4-Kinase Type III Alpha Involved in Enzymatic Activity and Hepatitis C Virus Replication. *J Virol* **88**:9909–9926.

doi:10.1128/jvi.01063-14

Hsu F, Hu F, Mao Y. 2015. Spatiotemporal control of phosphatidylinositol 4-phosphate by Sac2 regulates endocytic recycling. *J Cell Biology* **209**:97–110. doi:10.1083/jcb.201408027

Jović M, Kean MJ, Szentpetery Z, Polevoy G, Gingras A-C, Brill JA, Balla T. 2012. Two phosphatidylinositol 4-kinases control lysosomal delivery of the Gaucher disease enzyme, β-glucocerebrosidase. *Mol Biol Cell* **23**:1533–1545. doi:10.1091/mbc.e11-06-0553

Kay JG, Koivusalo M, Ma X, Wohland T, Grinstein S. 2012. Phosphatidylserine dynamics in cellular membranes. *Molecular Biology of the Cell* **23**:2198–2212. doi:10.1091/mbc.E11-11-0936

Kim Y, Guzman-Hernandez M, Balla T. 2011. A Highly Dynamic ER-Derived Phosphatidylinositol-Synthesizing Organelle Supplies Phosphoinositides to Cellular Membranes. *Developmental Cell* **21**:813–824. doi:10.1016/j.devcel.2011.09.005

Kim Y, Guzman-Hernandez M-L, Wisniewski E, Balla T. 2015. Phosphatidylinositol-Phosphatidic Acid Exchange by Nir2 at ER-PM Contact Sites Maintains Phosphoinositide Signaling Competence. *Dev Cell* **33**:549–561. doi:10.1016/j.devcel.2015.04.028

Lange Y, aisgood, Ramos B, Steck T. 1989. Plasma membranes contain half the phospholipid and 90% of the cholesterol and sphingomyelin in cultured human fibroblasts. *J Biological Chem* **264**:3786–93.

Lapetina EG, Michell RH. 1973. Phosphatidylinositol metabolism in cells receiving extracellular stimulation. *Febs Lett* **31**:1–10. doi:10.1016/0014-5793(73)80061-4

Lees JA, Messa M, Sun E, Wheeler H, Torta F, Wenk MR, Camilli P, Reinisch KM. 2017a. Lipid transport by TMEM24 at ER–plasma membrane contacts regulates pulsatile insulin secretion. *Science* **355**:eaah6171. doi:10.1126/science.aah6171

Lees JA, Zhang Y, Oh MS, Schauder CM, Yu X, Baskin JM, Dobbs K, Notarangelo LD, Camilli P, Walz T, Reinisch KM. 2017b. Architecture of the human PI4KIIIα lipid kinase complex. *Proc National Acad Sci* **114**:13720–13725. doi:10.1073/pnas.1718471115

LEES M, FOLCH J, STANLEY SG, CARR S. 1959. A SIMPLE PROCEDURE FOR THE PREPARATION OF BRAIN SULPHATIDES*. *J Neurochem* **4**:9–18. doi:10.1111/j.1471-4159.1959.tb13169.x

Lipsky N, Pagano R. 1985. A vital stain for the Golgi apparatus. *Science* **228**:745–747. doi:10.1126/science.2581316

Luo X, Wasilko DJ, Liu Y, Sun J, Wu X, Luo Z-Q, Mao Y. 2015. Structure of the Legionella Virulence Factor, SidC Reveals a Unique PI(4)P-Specific Binding Domain Essential for Its Targeting to the Bacterial Phagosome. *PLOS Pathogens* **11**:e1004965. doi:10.1371/journal.ppat.1004965

Ma Y, Taylor S. 2002. A 15-Residue Bifunctional Element in d-AKAP1 Is Required for Both Endoplasmic Reticulum and Mitochondrial Targeting. *J Biol Chem* **277**:27328–27336. doi:10.1074/jbc.m201421200

Martin O, Pagano R. 1987. Transbilayer movement of fluorescent analogs of phosphatidylserine and phosphatidylethanolamine at the plasma membrane of cultured cells. Evidence for a protein-mediated and ATP-dependent process(es). *J Biological Chem* **262**:5890–8.

Michell RH. 2018. Do inositol supplements enhance phosphatidylinositol supply and thus support endoplasmic reticulum function? *British Journal of Nutrition* **120**. doi:10.1017/S0007114518000946

Moser J, Gerstel B, Meyer J, Chakraborty T, Wehland J, Heinz DW. 1997. Crystal structure of the phosphatidylinositol-specific phospholipase C from the human pathogen Listeria monocytogenes11Edited by R. Huber. *J Mol Biol* **273**:269–282. doi:10.1006/jmbi.1997.1290

Nakanishi S, Catt K, Balla T. 1995. A wortmannin-sensitive phosphatidylinositol 4-kinase that regulates hormone-sensitive pools of inositolphospholipids. *Proc National Acad Sci* **92**:5317–5321. doi:10.1073/pnas.92.12.5317

Nakatsu F, Messa M, Nández R, Czapla H, Zou Y, rittmatter S, Camilli P. 2015. Sac2/INPP5F is an inositol 4-phosphatase that functions in the endocytic pathway. *The Journal of Cell Biology* **209**:85–95. doi:10.1083/jcb.201409064

Nasuhoglu C, Feng S, Mao Y, Shammat I, Yamamato M, Earnest S, Lemmon M, Hilgemann DW. 2002. Modulation of cardiac PIP2 by cardioactive hormones and other physiologically relevant interventions. *American Journal of Physiology - Cell Physiology* **283**:C223–C234. doi:10.1152/ajpcell.00486.2001

Olivo-Marin J-C. 2002. Extraction of spots in biological images using multiscale products. *Pattern Recogn* **35**:1989–1996. doi:10.1016/s0031-3203(01)00127-3

Olkkonen VM. 2015. OSBP-Related Protein Family in Lipid Transport over Membrane Contact Sites. *Lipid insights* **8**:1–9. doi:10.4137/LPI.S31726

Pagano R, Longmuir K, Martin O. 1983. Intracellular translocation and metabolism of a fluorescent phosphatidic acid analogue in cultured fibroblasts. *J Biological Chem* **258**:2034–40.

Quinn KV, Behe P, Tinker A. 2008. Monitoring changes in membrane phosphatidylinositol 4,5-bisphosphate in living cells using a domain from the transcription factor tubby. *J Physiology* **586**:2855–2871. doi:10.1113/jphysiol.2008.153791

Saheki Y, Bian X, Schauder CM, Sawaki Y, Surma MA, Klose C, Pincet F, Reinisch KM, DeCamilli P. 2016. Control of plasma membrane lipid homeostasis by the extended synaptotagmins. *Nature cell biology* **18**:504–515. doi:10.1038/ncb3339

Schindelin J, Arganda-Carreras I, Frise E, Kaynig V, Longair M, Pietzsch T, Preibisch S, Rueden C, Saalfeld S, Schmid B, Tinevez J-Y, White D, Hartenstein V, Eliceiri K, Tomancak P, Cardona A. 2012. Fiji: an open-source platform for biological-image analysis. *Nat Methods* **9**:676. doi:10.1038/nmeth.2019

Schmick M, Vartak N, Papke B, Kovacevic M, Truxius DC, Rossmannek L, Bastiaens PI. 2014. KRas Localizes to the Plasma Membrane by Spatial Cycles of Solubilization, Trapping and Vesicular Transport. *Cell* **157**:459–471. doi:10.1016/j.cell.2014.02.051

Shaner NC, Campbell RE, Steinbach PA, Giepmans BN, Palmer AE, Tsien RY. 2004. Improved monomeric red, orange and yellow fluorescent proteins derived from Discosoma sp. red fluorescent protein. *Nat Biotechnol* **22**:1567–1572. doi:10.1038/nbt1037

Sohn M, Korzeniowski M, Zewe JP, Wills RC, Hammond G, Humpolickova J, Vrzal L, Chalupska D, Veverka V, Fairn GD, Boura E, Balla T. 2018. PI(4,5)P2 controls plasma membrane PI4P and PS levels via ORP5/8 recruitment to ER–PM contact sites. *J Cell Biol* jcb.201710095. doi:10.1083/jcb.201710095

Struck D, Pagano R. 1980. Insertion of fluorescent phospholipids into the plasma membrane of a mammalian cell. *J Biological Chem* **255**:5404–10.

Subach OM, Cranfill PJ, Davidson MW, Verkhusha VV. 2011. An Enhanced Monomeric Blue Fluorescent Protein with the High Chemical Stability of the Chromophore. *Plos One* **6**:e28674. doi:10.1371/journal.pone.0028674

Szentpetery Z, Várnai P, Balla T. 2010. Acute manipulation of Golgi phosphoinositides to assess their importance in cellular trafficking and signaling. *Proc National Acad Sci* **107**:8225–8230. doi:10.1073/pnas.1000157107

Ting A, Pagano R. 1990. Detection of a phosphatidylinositol-specific phospholipase C at the surface of Swiss 3T3 cells and its potential role in the regulation of cell growth. *J Biological Chem* **265**:5337–40.

Traynor-Kaplan A, Kruse M, Dickson EJ, Dai G, Vivas O, Yu H, Whittington D, Hille B. 2017. Fatty-acyl chain profiles of cellular phosphoinositides. *Biochimica et biophysica acta* **1862**:513–522. doi:10.1016/j.bbalip.2017.02.002

Valm AM, Cohen S, Legant WR, Melunis J, Hershberg U, Wait E, Cohen AR, Davidson MW, Betzig E, Lippincottschwartz J. 2017. Applying systems-level spectral imaging and analysis to reveal the organelle interactome. *Nature* **546**:162–167. doi:10.1038/nature22369

Vance JE. 2015. Phospholipid Synthesis and Transport in Mammalian Cells. *Traffic* **16**. doi:10.1111/tra.12230

Vishwakarma RA, Vehring S, Mehta A, Sinha A, Pomorski T, Herrmann A, Menon AK. 2005. New fluorescent probes reveal that flippase-mediated flip-flop of phosphatidylinositol across the endoplasmic reticulum membrane does not depend on the stereochemistry of the lipid. *Organic & Biomolecular Chemistry* **3**:1275–1283. doi:10.1039/B500300H

Wang L, Iwasaki Y, Andra KK, Pandey K, Menon AK, Bütikofer P. 2018. Scrambling of natural and fluorescently tagged phosphatidylinositol by reconstituted G protein–coupled receptor and TMEM16 scramblases. *Journal of Biological Chemistry* **293**:18318–18327. doi:10.1074/jbc.RA118.004213

Weber S, Wagner M, Hilbi H. 2014. Live-Cell Imaging of Phosphoinositide Dynamics and Membrane Architecture during Legionella Infection. *Mbio* **5**:e00839-13. doi:10.1128/mbio.00839-13

Willars G, Nahorski S, Challiss R. 1998. Differential regulation of muscarinic acetylcholine

receptor-sensitive polyphosphoinositide pools and consequences for signaling in human neuroblastoma cells. *The Journal of biological chemistry* **273**:5037–46.

Yadav S, Garner K, Georgiev P, Li M, Gomez-Espinosa E, Panda A, Mathre S, Okkenhaug H, Cockcroft S, Raghu P. 2015. RDGBα, a PtdIns-PtdOH transfer protein, regulates G-protein-coupled PtdIns(4,5)P2 signalling during Drosophila phototransduction. *J Cell Sci* **128**:3330–3344. doi:10.1242/jcs.173476

Zewe JP, Wills RC, Sangappa S, Goulden BD, Hammond GR. 2018. SAC1 degrades its lipid substrate PtdIns4P in the endoplasmic reticulum to maintain a steep chemical gradient with donor membranes. *eLife* **7**. doi:10.7554/eLife.35588

Figure Legends

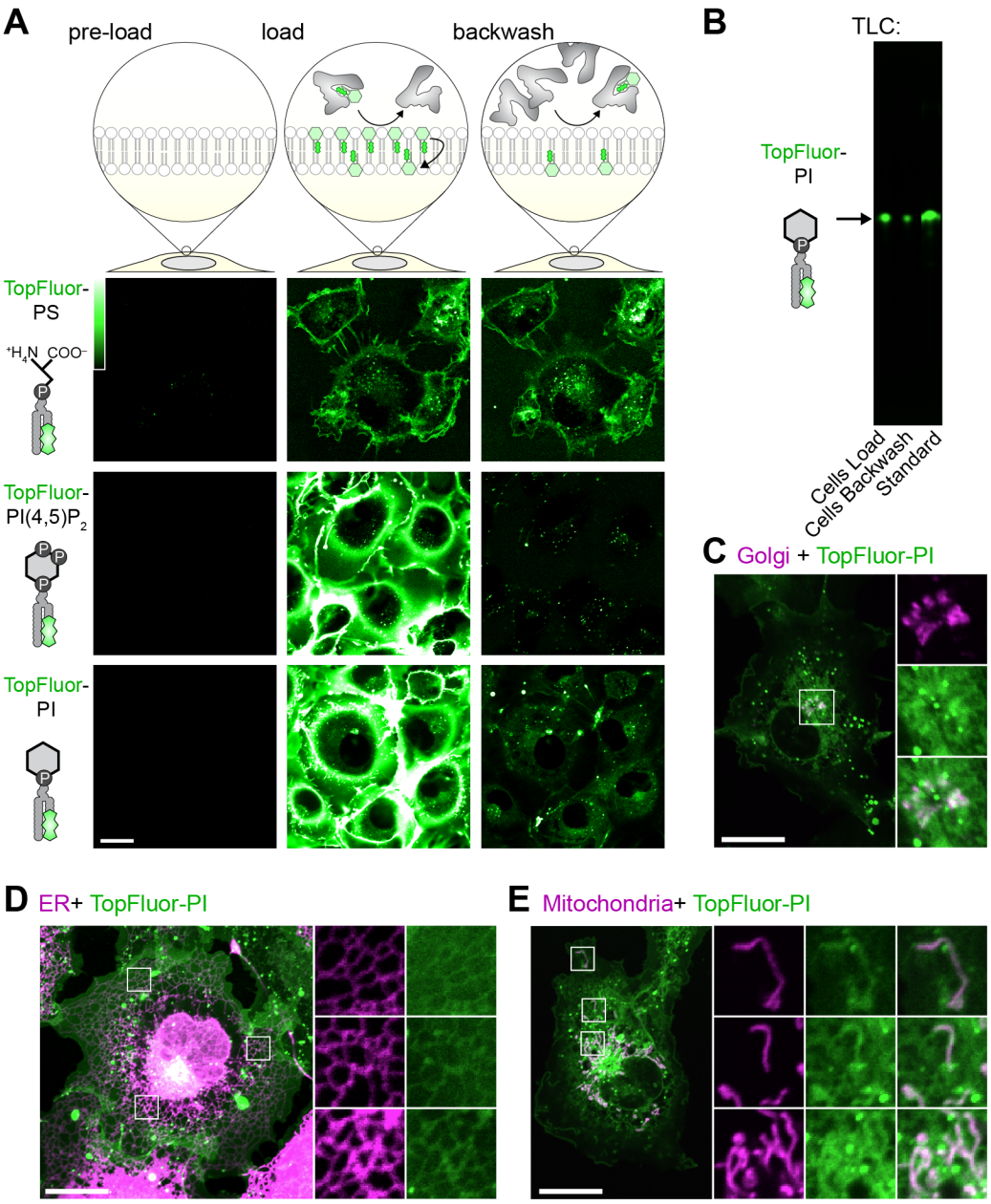

Figure 1: Fluorescent PI is not enriched at the PM. (**A**) **Internalization of fluorescent lipids**. COS-7 cells were loaded at 37˚C with the indicated acyl-conjugated TopFLuor lipids complexed with BSA. After 15 min, a 20-fold excess of un-complexed BSA was used to back-extract lipid remaining in the outer PM leaflet. (**B**) **Loaded TopFluor-PI is not metabolized**. COS-7 cells were loaded or loaded and back-extracted as in A. Lipids were then extracted and resolved by thin-later chromatography. (**C-E**) **Loaded TopFluor-PI labels the Golgi** (C)**, ER** (D) **and mitochondria** (E). COS-7 cells that had been transfected with mCherry-β4-GalT^{N82} (C), iRFP-Sec61β (D) or COX8A^{N19}x2-mCherry (E) were loaded and back-extracted as in (A). Scale bar = 20 μm in all panels; insets are 10.9 μm (C) or 7.3 μm (D-E). Data are representative of three or more experiments.

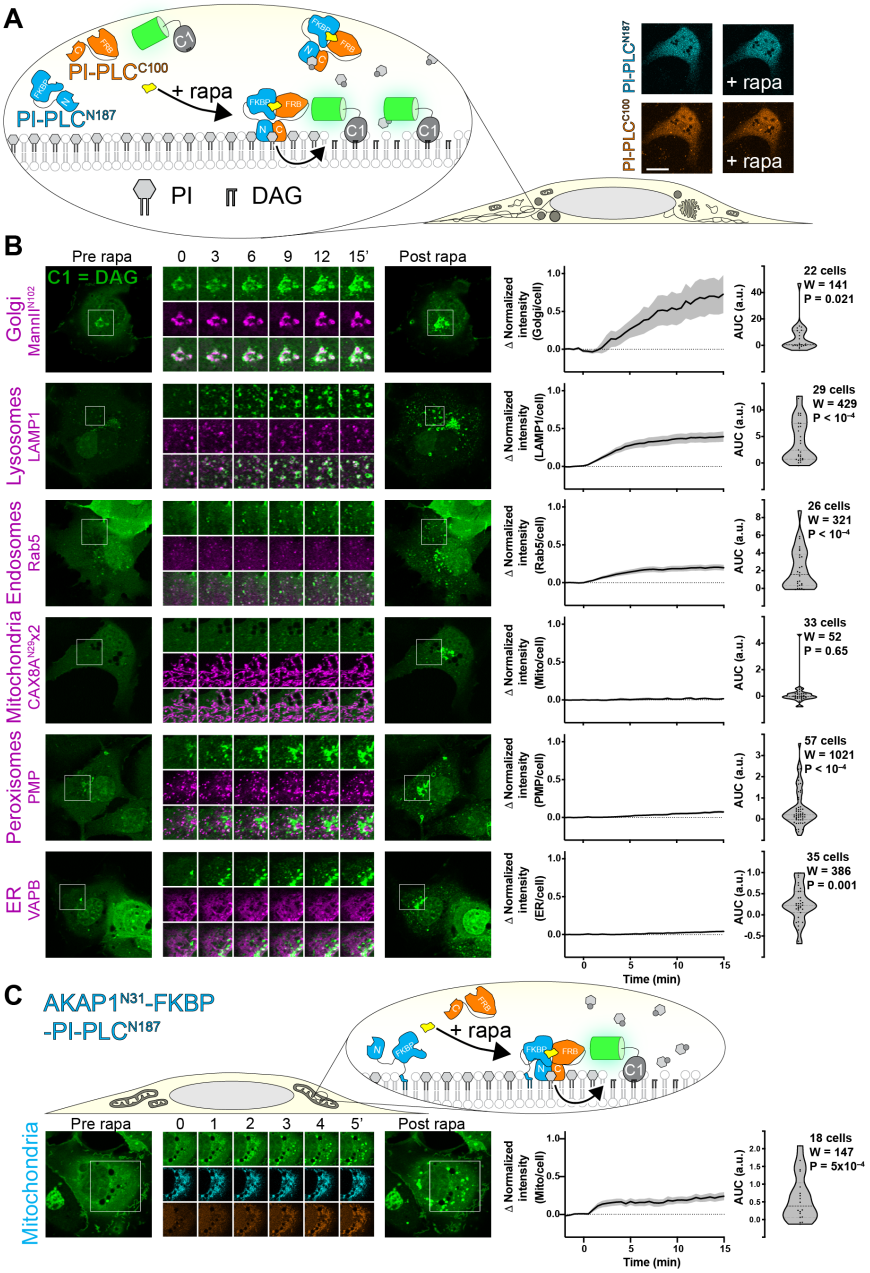

Figure 2: Chemically-induced dimerization of a split PI-PLC induces intracellular accumulation of DAG. (**A**) **Experimental set-up:** Rapamycin-induced dimerization of FKBP-fused N-terminal 187 residues of PI-PLC (cyan) with the FRB-fused C-terminal 100 residues (orange) reconstitutes the active enzyme, though no visibly change in the cytosolic localization of the TagBFP2/iRFP-fused enzyme fragments is observed (confocal Images at right). (**B**) **DAG accumulation on cytosolic leaflets of intracellular organelles**, with the greatest increases in the Golgi and endo/lysosomal compartments. No or comparatively minor changes are observed in mitochondria, peroxisomes or the ER. Cells were expressing GFP-PKD1-C1ab to detect DAG, the indicated organelle markers (magenta), FKBP-PI-PLC^{N187} and FRB-PI-PLC^{C100} (not shown); they were treated with 1 μM rapamycin at time 0. Inset regions are 15 μm. (**C**) **Anchoring PI-PLC^{N187} to the mitochondrial outer membrane shows transient accumulation of DAG after recruitment of PI-PLC^{N100}**. Cells were transfected as in B, but with AKAP^{N31}—fused PI-PLC^{N187} replacing the unanchored version in B. In both B and C, the curves at right show the mean change in C1ab reporter intensity at each compartment, with s.e.m. shaded. The violin plots show area under the curve, with the number of cells (pooled across 3-6 independent experiments), the sum of signed ranks (W) and P-value from a two-tailed Wilcoxon signed rank test comparing to a null hypothesis area under the curve value of 0.

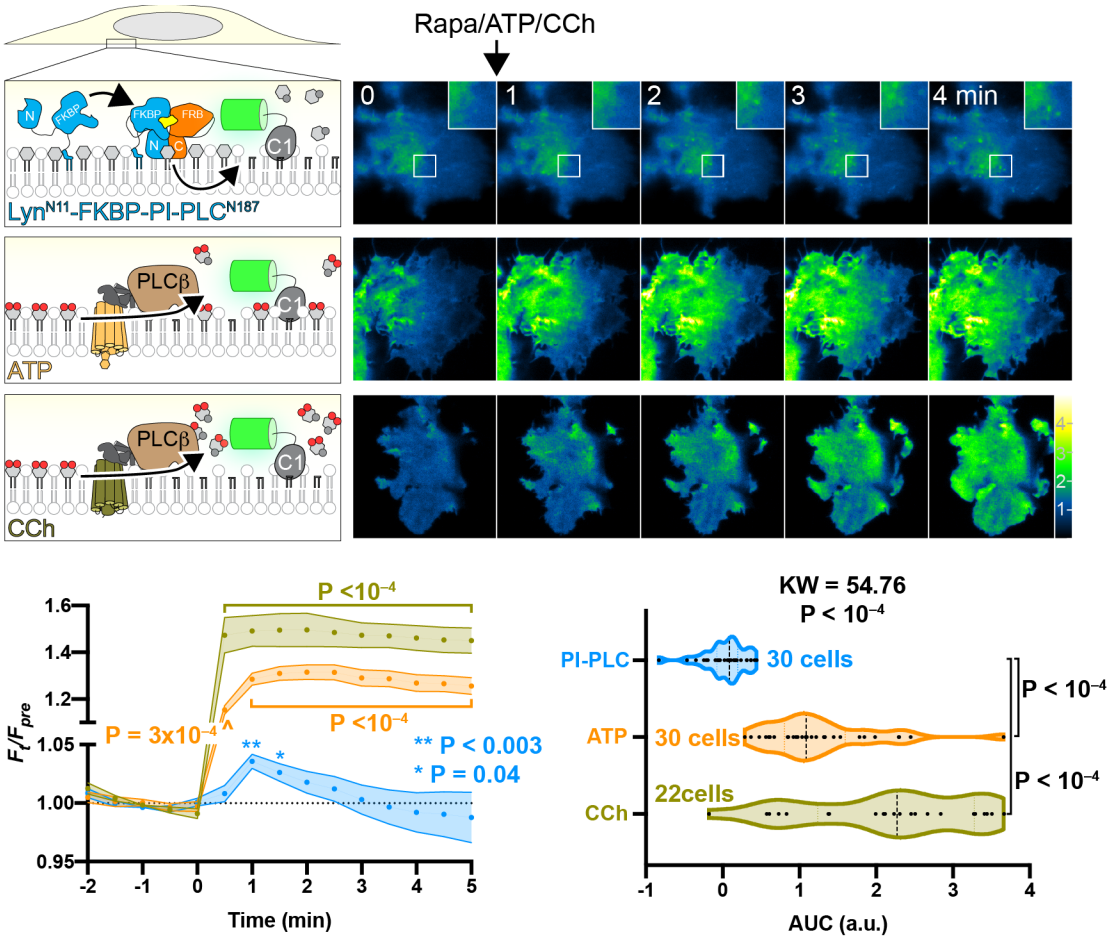

Figure 3: PM-specific dimerization of split PI-PLC induces very little DAG compared to PI(4,5)P_2-specific PLC. Cells were transfected with PI-PLC^{C100}-FRB, PM-targeted Lyn^{N11}-FKBP-PI-PLC^{N100} and GFP-PKD1-C1ab to detect DAG. Rapamycin was used to induce PI-PLC reconstitution at the PM, or else endogenous PLCβ was activated by G_q-coupled agonists ATP (to activate endogenous P2Y receptors) or carbachol (CCh, to activate over-expressed muscarinic M3 receptors). TIRFM images are color-coded to represent fluorescence intensity relative to pre-stimulus levels (F_t/F_{pre}) as indicated. Inset region is 5 μm. The line graphs show mean F_t/F_{pre} with s.e.m. shaded; P values are derived from Dunn's multiple comparison test comparing to time 0, following Friedman's test (Friedman statistic = 49.16, PI-PLC, P = 0.045; 497.0, ATP, P < 10^{-4}; 282.3, CCh; P < 10^{-4}). Where not indicated, the P value from Dunn's > 0.05. The violin plots show area under the curve analysis of the line graphs with the number of cells from 3 independent experiments, with results of a Kruskal-Wallis test and P values from a post-hoc Dunn's multiple comparison test indicated.

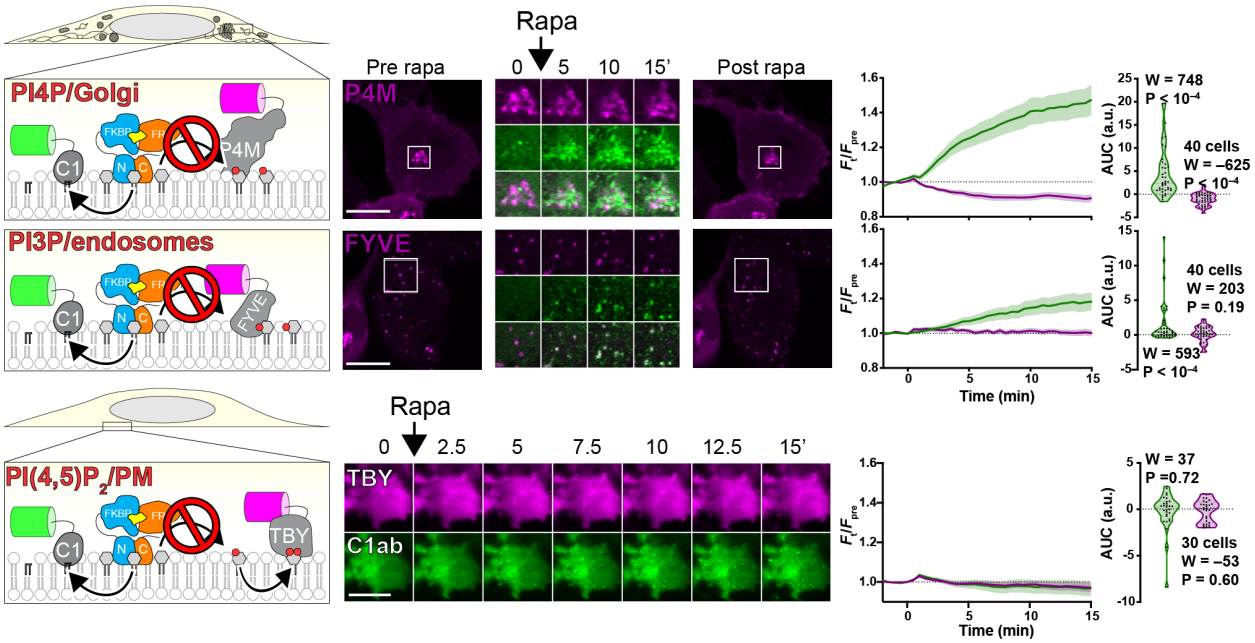

Figure 4: PI-PLC leads to little or no depletion of PPIn. Cells were transfected with PI-PLC^{C100}-FRB, FKBP-PI-PLC^{N100} (or PM-targeted Lyn^{N11}-FKBP-PI-PLC^{N100}) and GFP-PKD1-C1ab to detect DAG, along with the indicated PPIn biosensor. Dimerization and activation of PI-PLC was induced with 1 μM rapamycin as indicated. Images are confocal sections, except for the PM images which are TIRFM. Scale bars = 20 μm. Line graphs show the change in compartment specific fluorescence of C1ab or the PPIn biosensor normalized to pre-rapamycin levels (F_{pre}). The violin plots show area under the curve, with the number of cells (pooled across 3 independent experiments), the sum of signed ranks (W) and P-value from a two-tailed Wilcoxon signed rank test comparing to a null hypothesis area under the curve value of 0 (with a baseline of 1).

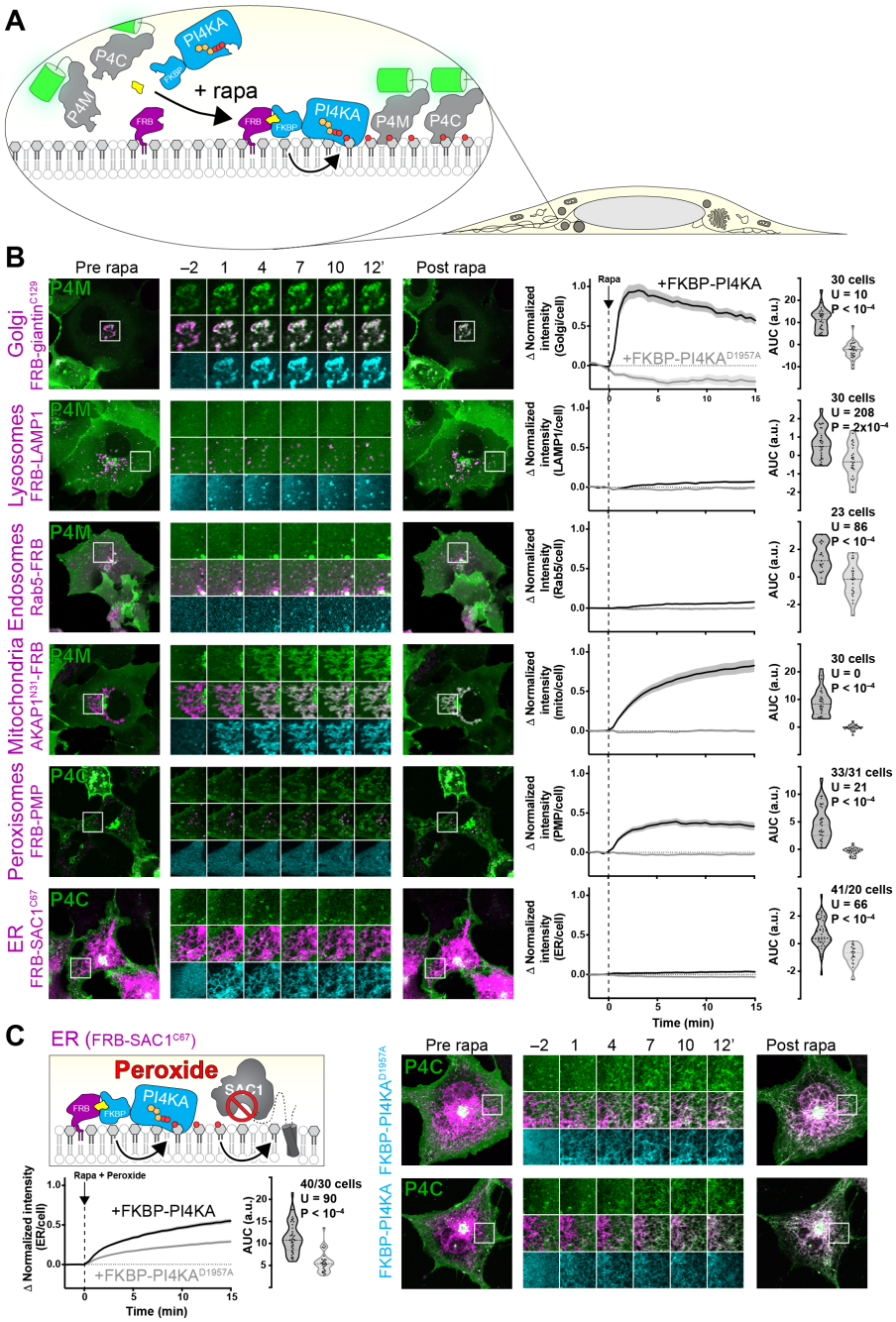

Figure 5: Compartment-specific recruitment of PI4KA reveals intracellular PI pools. (**A**) **Experimental set-up:** Rapamycin-induced recruitment of FKBP-PI4KA^{N1001} by dimerization with compartment-specific FRB to induce PI4P synthesis from endogenous PI, revealed with GFP-P4M or -P4C. (**B**) **PI4P accumulation on cytosolic leaflets of intracellular organelles**, with the greatest increases in the Golgi and mitochondria, with barely detectable increases in endosomes and ER. Peroxisomes show a large increase, but PI4P intensity also occurs outside of PMP-marked compartments. Cells are expressing GFP-P4M or -P4C (green), compartment-specific FRB (magenta) and FKBP-PI4KA^{N1001} (cyan) as indicated were treated with 1 μM rapamycin at time 0. Inset regions are 15 μm. The line graphs at right show the mean change in PI4P reporter intensity at each compartment, with s.e.m. shaded. The violin plots show area under the curve analysis of the curves, with the number of cells (pooled across 2-4 independent experiments), Mann-Whitney U statistic and P-value from a two-tailed test. (**C**) **Peroxide-mediated inhibition of ER-associated SAC1 PI4P phosphatase** reveals an endogenous pool of PI that can be converted to PI4P. Experiment and data are identical to (B), except cells were treated with 500 μM hydrogen peroxide in addition to rapamycin.

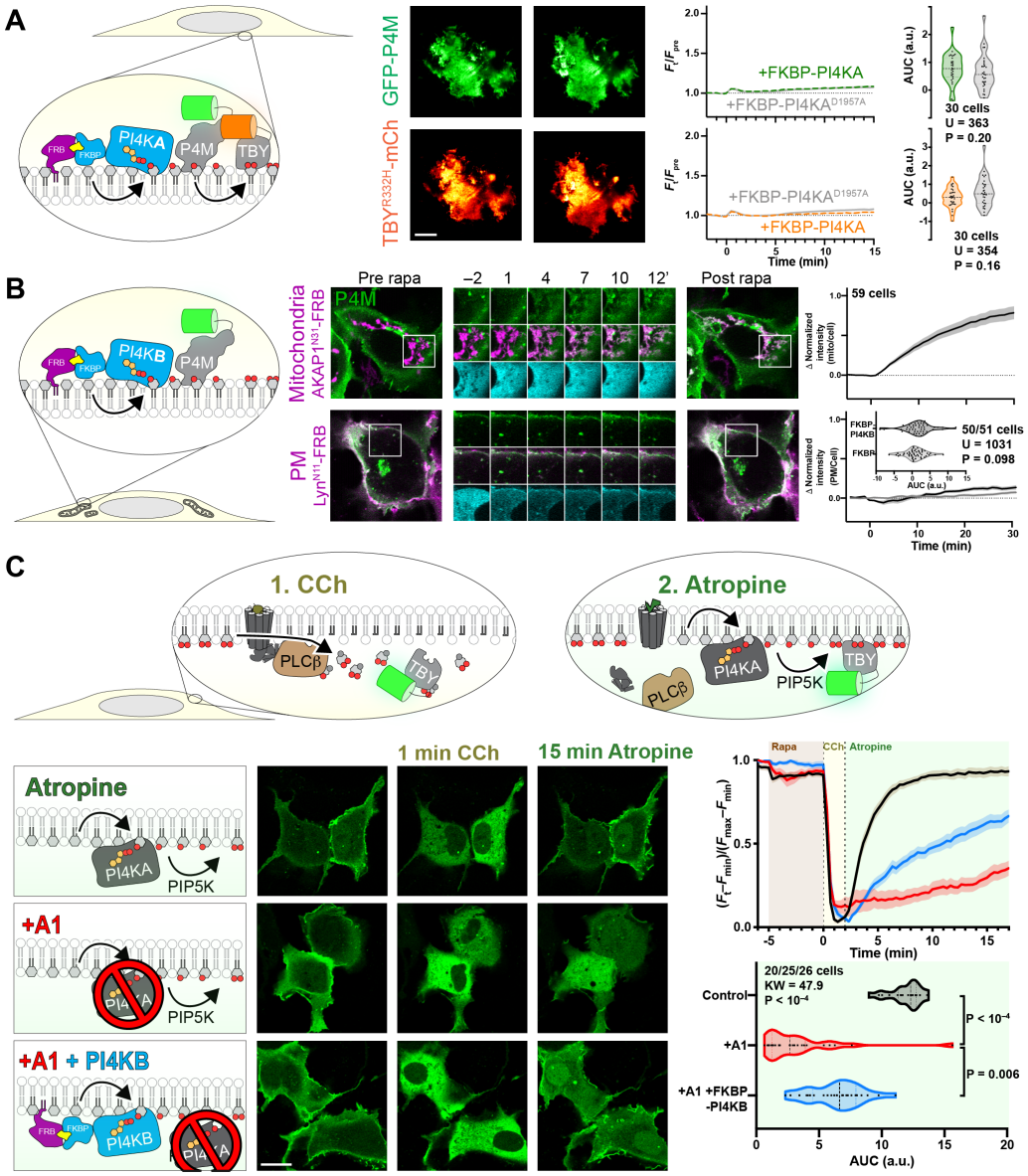

Figure 6: Recruitment of PI4K to the PM reveals a scarcity of PI. (**A**) **Recruitment of PI4KA^{N1001} shows no increase in PI4P or PI(4,5)P$_2$.** COS-7 cells imaged by TIRF expressing GFP-P4Mx1 or Tubby$_c$-mCherry together with FKBP-PI4K^{N1001} and Lyn^{N11}-FRB were treated with 1 μM rapamycin at time 0 to induce dimerization. Scale bar = 20 μm. The curves at right show the mean change in reporter intensity, with s.e.m. shaded. The violin plots show area under the curve analysis of the curves, with the number of cells (pooled across 3 independent experiments) and the Mann-Whitney U statistic and P-value from a two-tailed test. (**B**) **PI4KB induced PI4P increases at the mitochondria but no the PM**. COS-7 cells transfected with P4Mx1 to detect PI4P increases by confocal microscopy in conjunction with the indicated compartment-specific FRB and FKBP-PI4KB. Insets are 15 μm. Line graphs are means with s.e.m. shaded; inset violin plot shows area under the curve analysis, with number of cells (pooled across 3 independent experiments) and the Mann-Whitney U statistic and P-value from a two-tailed test. (**C**) **PI4KB is active in the PM**. COS-7 cells were co-transfected with muscarinic M3 receptors to stimulate PLCβ-induced PI(4,5)P$_2$ and PI4P depletion from the PM in response to carbachol treatment. Subsequent treatment with the muscarinic antagonist atropine induces re-synthesis of PI4P and PI(4,5)P$_2$ via endogenous PI4KA. Where indicated 30 nM of the PI4KA inhibitor A1 were added. Images show confocal sections (bar = 20 μm) before stimulation, after addition of carbachol and after atropine addition as indicated. Curves are means with s.e.m. shaded. The violin plot shows area under the curve analysis for the post-atropine addition, with number of cells (three independent experiments), Kruskall Wallace statistic and P value from a two-tailed test. P values between individual groups show are derived from a post-hoc Dunn's multiple comparison test.